DCATT Source, Simulator and Wavefront Sensor Camera

Preliminary Performance Assessment

David Redding, Scott Basinger, Andrew E. Lowman

draft of 3/8/99

1.   Overview

This memo documents the performance of the NGST DCATT Source, Simulator, Wavefront Sensor Camera modules, and the DCATT Executive control software, as determined by testing at JPL. This testing included closed-loop operations, wherein aberrations introduced into the telescope simulator deformable mirror (DM) were sensed using the WF sensor camera and removed by actuation of the DM. The testing was performed using an abbreviated configuration of the DCATT hardware, as described below.

Optical wavefront (WF) error performance exceeded requirements and expectations. Uncompensated WF quality is at the ⁄10 level, and the actively corrected WF error is better than ⁄30 (RMS) and ⁄5 (P-V). Some effort was made to determine individual component error contributions to the overall WF error performance. Detection noise, various WF sensing error factors, DM actuation error were varied and their sensitivities recorded. WFE performance was limited by the DM spatial resolution and actuation error, and will improve after integration with the AO bench module, with its higher-resolution 349-actuator DM.

2.   Optical configuration

The overall DCATT optical configuration is illustrated on Fig. 1. As shown, it consists of 5 major hardware modules: the Source; the Simulator; the AO Bench; the Telescope; and the WF Sensor Camera. The AO bench and segmented mirror telescope modules are being implemented at GSFC and were not available for this round of testing. For these tests, the Source, Simulator and WFS Camera modules were integrated by placing the WFS at the output of the simulator, where the AO bench would normally be (Fig. 2).
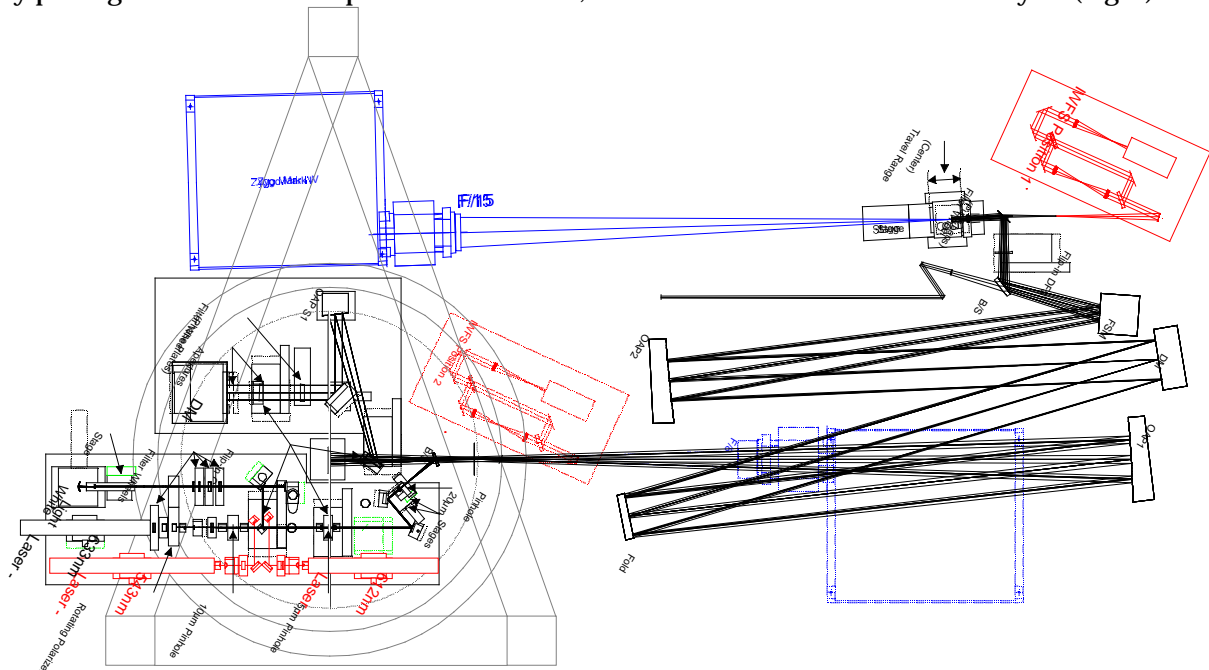

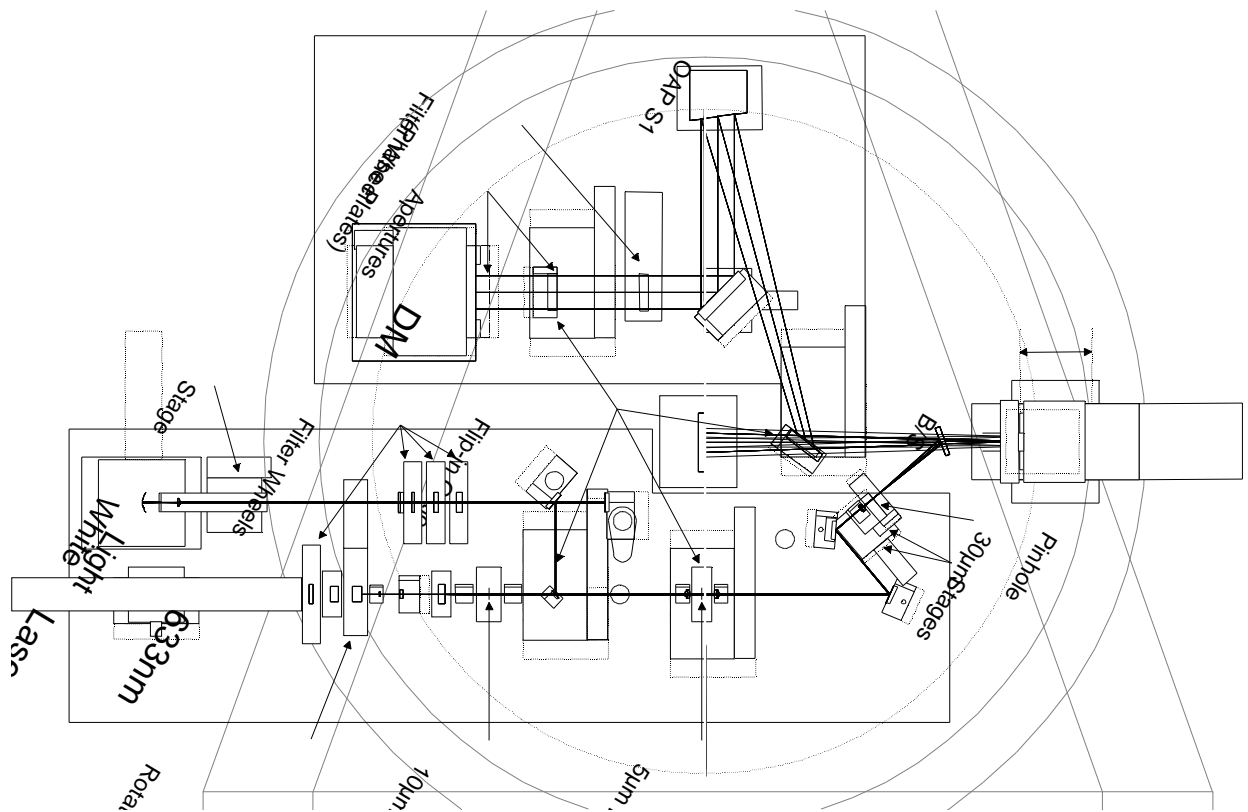
Figure 1. DCATT optical layout.

Figure 2. Source/Simulator/WF Sensor configuration.

Each module is enclosed and internally baffled by anodized aluminum plates attached to a skeleton frame. The covers can be removed for access.

2.1 Source module

The Source module layout is shown in Fig. 3, and a photo of the lab setup highlighting the source is provided in Fig. 4. Detailed description of the Source is provided in Ref. 1. The source is controlled locally by the Optics Control Computer (Ref. 2) which also functions as a server for use during experiments by the Executive Computer (Ref. 3).The source module provides a choice of light sources: a 632.8 nm wavelength HeNe laser or a Xenon arc lamp with a selection of different spectral, bandwidth, and neutral density filters. Two additional lasers will be added to support operation of the Interferometic WFS planned for use as a scoring sensor.

The source output beam is defined by 2 pinholes and various element apertures. The first pinhole is located immediately after the white light source selector mirror. Acollimated input beam is focussed onto the pinhole by an $f/2.2$ lens. The pinhole size is nominally 5 um. The beam is then recollimated and relayed, after being clipped by the aperture of the pinhole lens mount. It is refocussed after passing through a 1.3 mm aperture, which defines an f/15 beam at the source output. At this location is a second pinhole, nominally 25 um. It acts as a spatial filter to remove Fresnel diffraction rings induced by the preceding apertures (Fig. 5). The nominal beam out of the source is thus a smooth, truncated Gaussian in profile, with the power at the edge about half that at the core.

Pupil images showing illumination profiles for 4 different pinhole configurations are shown in Fig. 5. Figure 5 also indicates power levels: these are not to be directly compared, as they were taken at different times, with different white light source bulbs and different alignments. Configurations tested to date are:

1. Nominal, with 5 um pinhole reimaged onto a 25 um pinhole at the source. Pupil illumination is shown at upper left in Fig. 5.

2. Intermediate taper, provided by replacing the 25 um pinhole at the output of the source with a 30 um pinhole. Not significantly different from the previous case, not illustrated.

3. Intermediate taper, provided by replacing the 25 um pinhole at the output of the source with a 50 um pinhole. The output beam taper is reduced, but residual diffraction effects flatten the wings of the focussed beam. Shown at upper right in Fig. 5.

4. Diffracted uniform beam. Completely removing the output pinhole gives a flatter beam on average, but with prominent diffraction rings. Lower left in Fig. 5.

5. Uniform beam. By completely removing the first pinhole and using a 5 um pinhole at the output of the source, the output beam becomes essentially uniform, at a reduced power level. Lower right in Fig. 5.
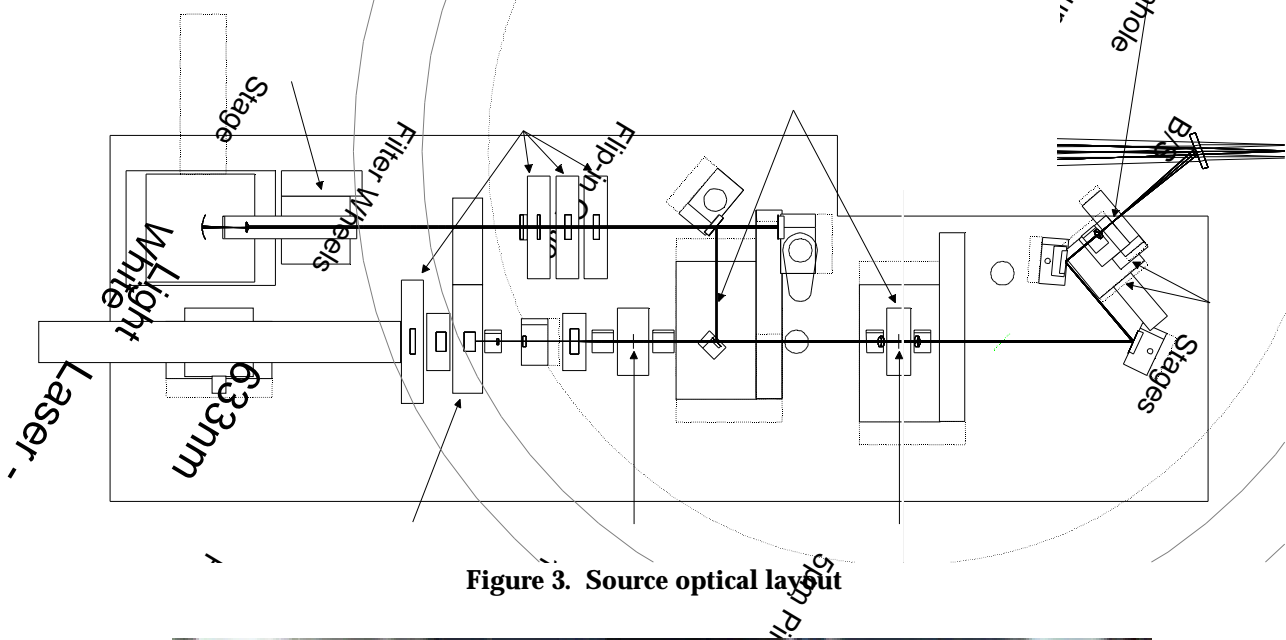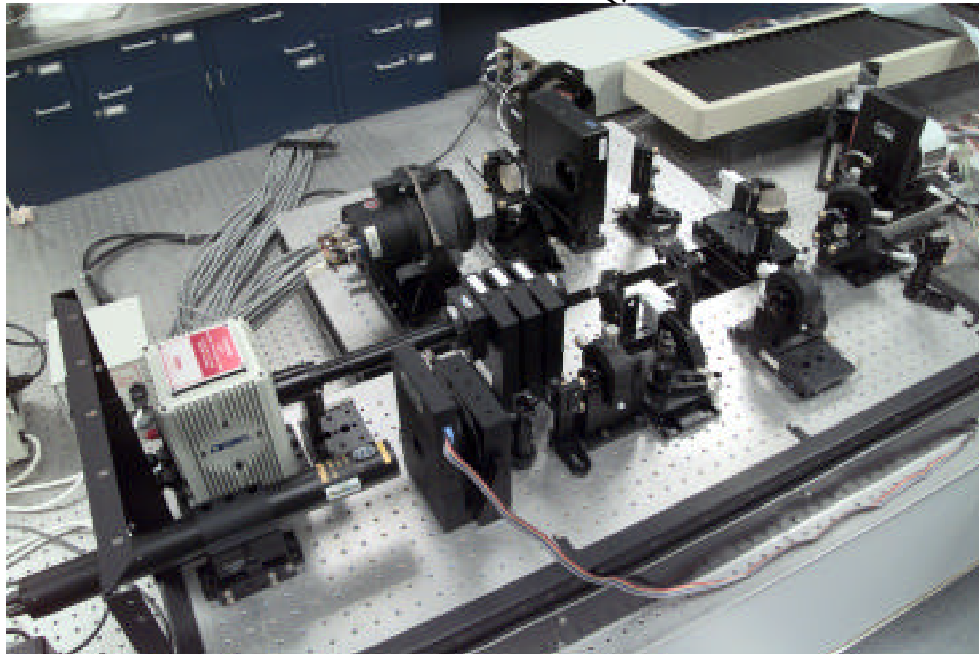

Figure 3. Source optical layout

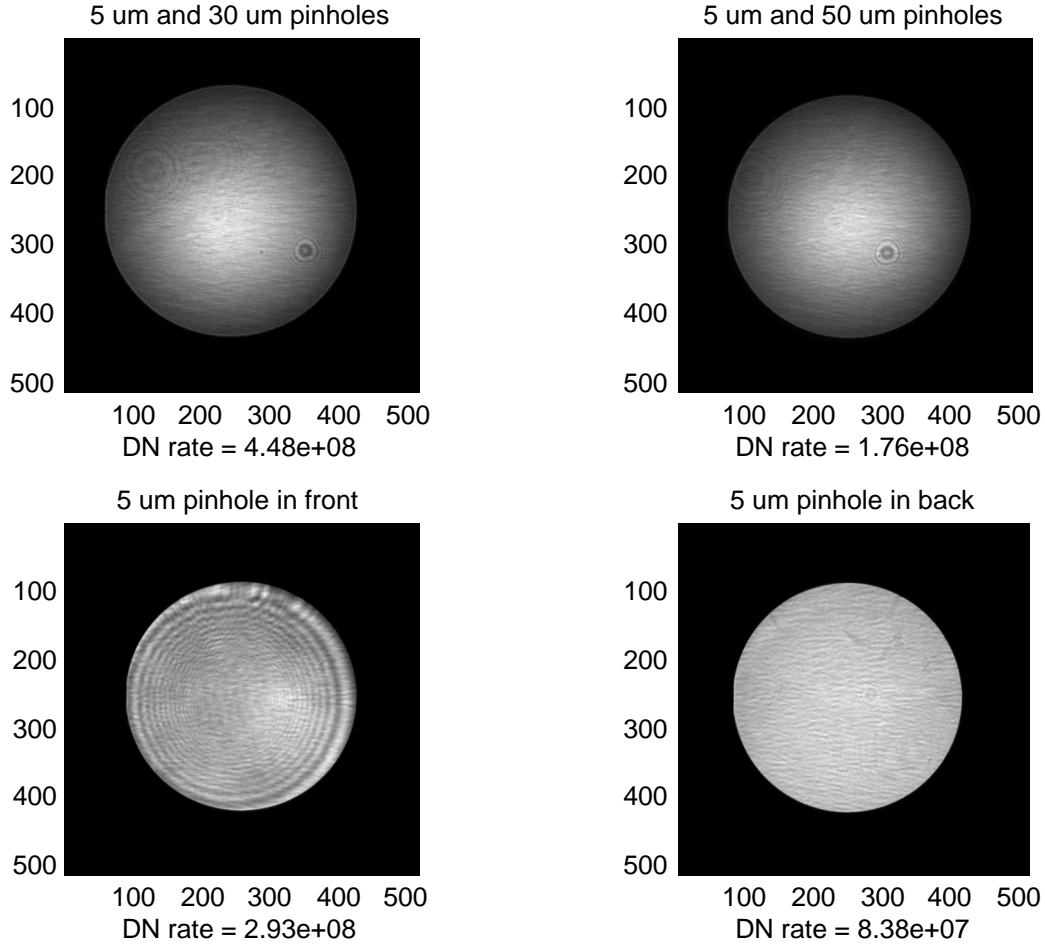Figure 4. Photograph of test configuration showing the source module

Figure 5. Source profile for various pinhole configurations

2.2 Telescope Simulator Module

The telescope simulator module is illustrated in Fig. 6. and described in detail in Ref. 4. A photograph showing the simulator is provided in Fig. 7.

The simulator consists of a pickoff mirror on a translating mount, which allows interception of the beam that feeds the telescope; an off-axis parabola which collimates the beam and reimages the pupil; a deformable mirror, located at the pupil; and a filter wheel which will contain a selection of phase plates for creating discontinuities in the pupil such as are provided by the segmented telescope. The simulator is intended as an aberrator, providing test problems for the WF control system.

The deformable mirror is an old Itek 97-actuator unit, originally intended for a Shuttle-based beam control experiment (Ref. 6). The DM electronics are a custom design (Ref. 7). DM actuator pitch is 7 mm; maximum stroke attainable with the electronics is approximately 2.6um. The stroke difference between adjacent actuators is limited in software to 1um, to avoid overstressing the mirror (Ref. 2). DM actuator commands are set in the Init Panel or the WF Control Panel of the Executive Computer (Ref. 3).

The DM aperture is stopped down to about 2.3 cm: this aperture defines the beam extent ($f/16$). It limits the number of useful actuators to 52, with about 6x6 actually in the beam. The aperture is decentered slightly to minimize the impact of a single bad actuator, located outside the clear aperture. Individual actuator influence functions were measured as described later in Section 6.
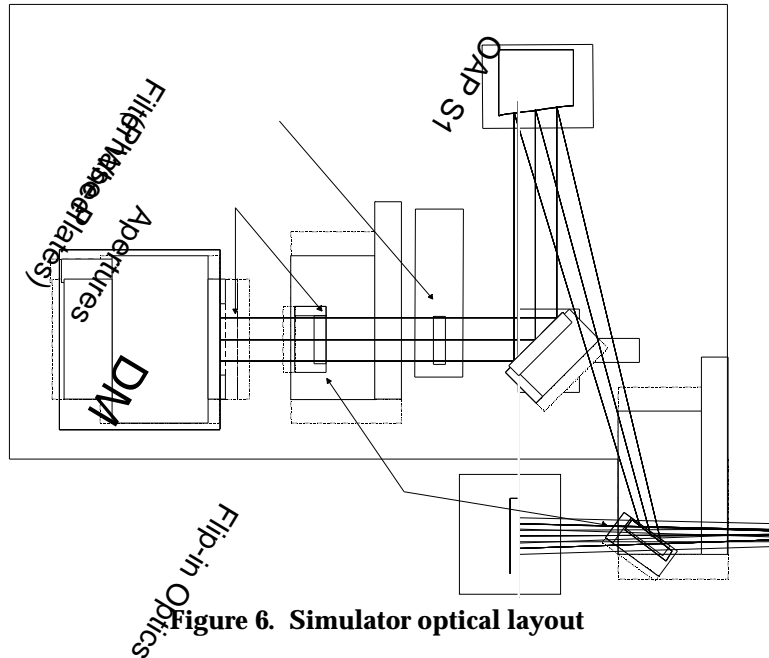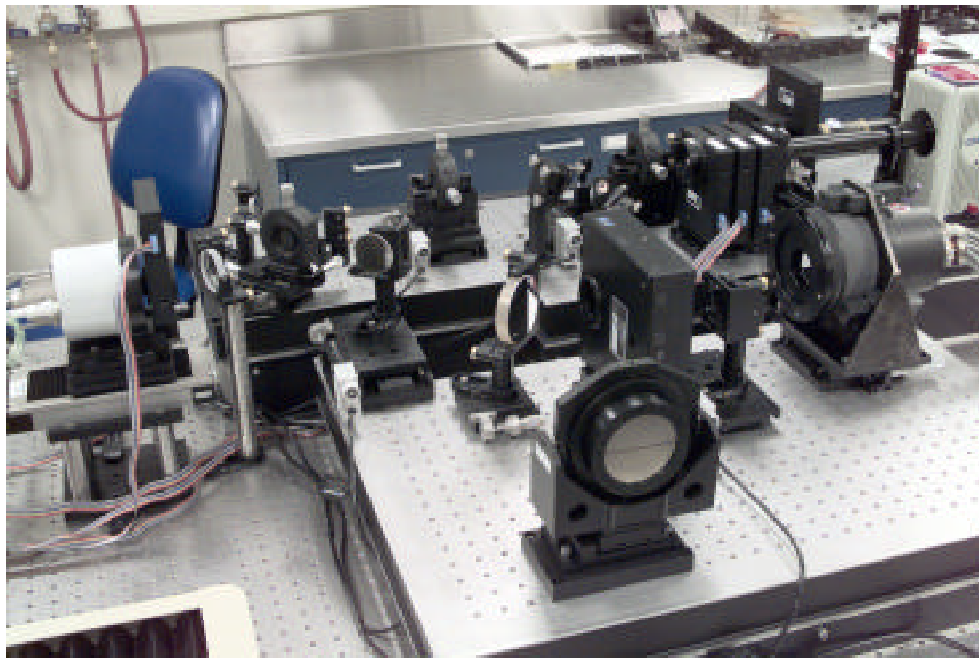
Figure 6. Simulator optical layout

Figure 7. Photograph of test confi guration showing simulator module

2.3   Wavefront Sensor

The wavefront sensor module consists of a camera mounted on a translation stage, with an internal camera shutter and a motorized filter wheel holding a pupil imaging lens. The translation stage is used to move the camera to take defocussed images for phase and prescription retrieval. The pupil imaging lens is inserted when an image of the exit pupil is desired; it remains outside the beam while focal imagery is being taken. Details of the design are given in Ref. 5.

The camera is a Photometrics Series 300, with a Kodak 1600 CCD chip recording the images. The chip uses 9 um square pixels in a 1536x1024 format. Full well for the chip is 85,000e-; equipped with a 14-bit A/D converter, its maximum dynamic range is 1:16,384, attainable by binning pixels. Without binning, read noise of 18 e- limits dynamic range to approximately 12 bits (1:4096). The camera is actively cooled with a built-in thermoelectric cooler and recirculating liquid coolant system. This combination maintains a temperature of -40 C, resulting in low dark current generation of 0.07 e-/pixel/sec. Note that the camera cannot be operated without the liquid circulation.
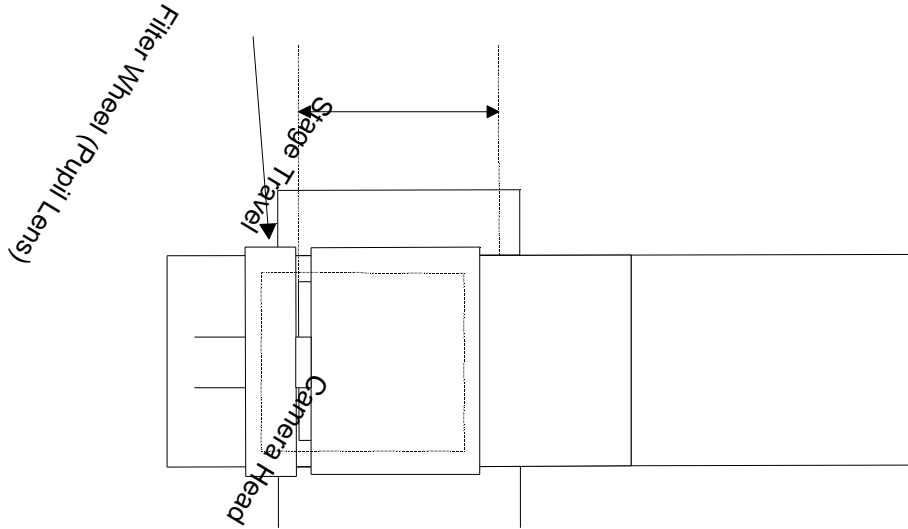

Figure 8. W avefront Sensor Camera optical layout

3. Example experiment

DCATT experiments typically begin by deliberately aberrating some aspect of the optics, and then using the various functions of the NGST baseline WF control to identify and correct the aberrations (Ref. 8). In the current configuration, aberrations are both introduced and corrected by the Simulator DM, utilizing the Fine Phasing control functions. This section walks through this process in some detail for one particular example case.

Experiments are defined and controlled using the DCATT Executive software (Ref. 3). The Executive provides a series of graphical control panels from which all hardware functions can be implemented. The Executive is activated by the user opening Matlab in the user's `/home/(username)/dcatt/executive` directory. At the Matlab ">" prompt, the user types "`gogui`," and the DCATT Init Panel appears (Fig. 9).

The Init Panel is the Executive "master" panel, from which each major function of DCATT (and of the baseline WF control) is accessed. Here the user selects the source type, laser or white light, and the initial DM setting. Different hardware configurations -- Telescope or Simulator, AO Bench or no -- are specified. The user also selects the target plant -- either "`hardware`" or "`model`." The `hardware` selection means that all functions will be performed on the actual DCATT hardware in the lab. The `model` selection means that all functions will be carried out in simulation. Upon selecting `hardware`, commands are sent to the OCC to open communications and initiate operations with the DCATT hardware modules. If `model` is selected, the DCATT Model Server is activated instead, and communications will be routed to the DCATT computer simulator. If neither `hardware` nor `model` is selected, embedded models will be used in place of the hardware.

The Init Panel provides access to all other DCATT control functions. A typical experiment in the final configuration will use the Aberrate functions to misalign and deform the PM and DM optics, in accordance with a particular statistical description of the hardware. The Coarse Align panels are then used to capture and align the various segments individually. The Coarse Phasing functions cophase all of the

segments, to less than 1 wave of error. The Fine Phasing panels then are used to perform wavefront sensing and control, to set the segments and/or the DMs to achieve the targeted final WF performance.

The Coarse Align and Coarse Phasing Panels are not needed in the current configuration, as the segmented telescope is not yet implemented in hardware (all phases of control can be exercised using the model setting). Other functions that are very useful now include the Snapshot panels (similar to the Data Acquisition panel described below) and the Calibrate panels.
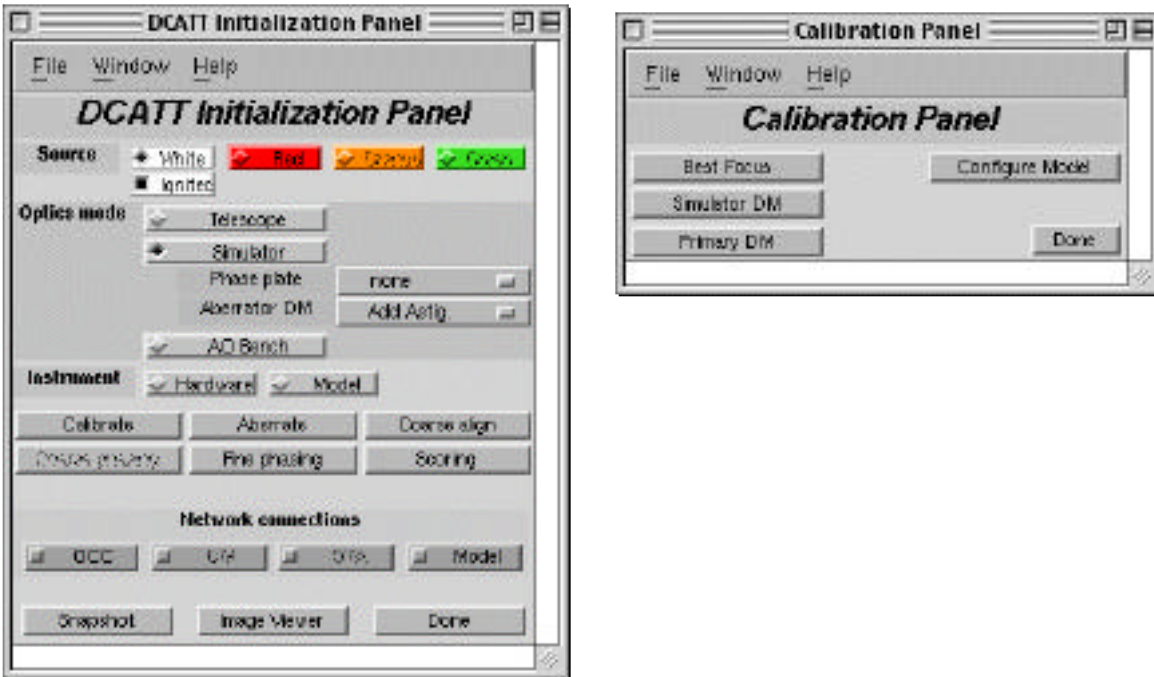

Figure 9. DCATT Init and Calibrate Panels

Pushing the "Calibrate" button opens a panel wherein several automated calibration functions can be initiated (Fig. 9). These include finding and recording the best focus position of the camera and determination of the DM influence functions. Snapshots of these panels are provided in Fig. 10. The Focus panel controls the WF camera stage, searching for best focus using a staged encircled energy metric similar to that used in Coarse Alignment. The DM panel automates the taking of WF sensor data for determining DM influence functions. The Model panel controls various noise and other settings for the simulated version of DCATT. Calibration functions need be performed only infrequently, to determine settings for the various hardware functions. We found it necessary to recalibrate focus only after major realignment.

For this example, the white light source was selected. The simulator DM was first set to "half," which drove each actuator to half of its full voltage, and then to "add astigmatism," which moved the actuators to increase the aberrations slightly. Internal limits were such that "half" was about 100 V. The objective was then to sense the wavefront error and correct it using the simulator DM. This is done using the Fine Phasing control mode.

The Fine Phasing functions are accessed by pressing the button by that name on the Init panel. This brings up the Fine Phasing Control Panel (Fig. 11). As shown, there are 3 main Fine Phasing functions: Data Acquisition, which is used to take images for phase retrieval processing; WF Sensing, which is used to perform the phase retrieval estimation of the wavefront; and WF Control, which operates on the WF estimate to determine segment and DM actuator commands that will reduce WF error.

The Data Acquisition panel (Fig. 11) allows the user to specify a complete set of up to 5 images for phase retrieval, including focal and pupil images at one or more different wavelengths, with dark subtraction and multiple frame integration. It has an exposure time calculator that ensures each frame is run to just below saturation. It has provision for specifying different defocus settings, which are implemented by

translating the WFS camera. It stores all of the data for a particular session in Matlab ".mat" format datafiles.
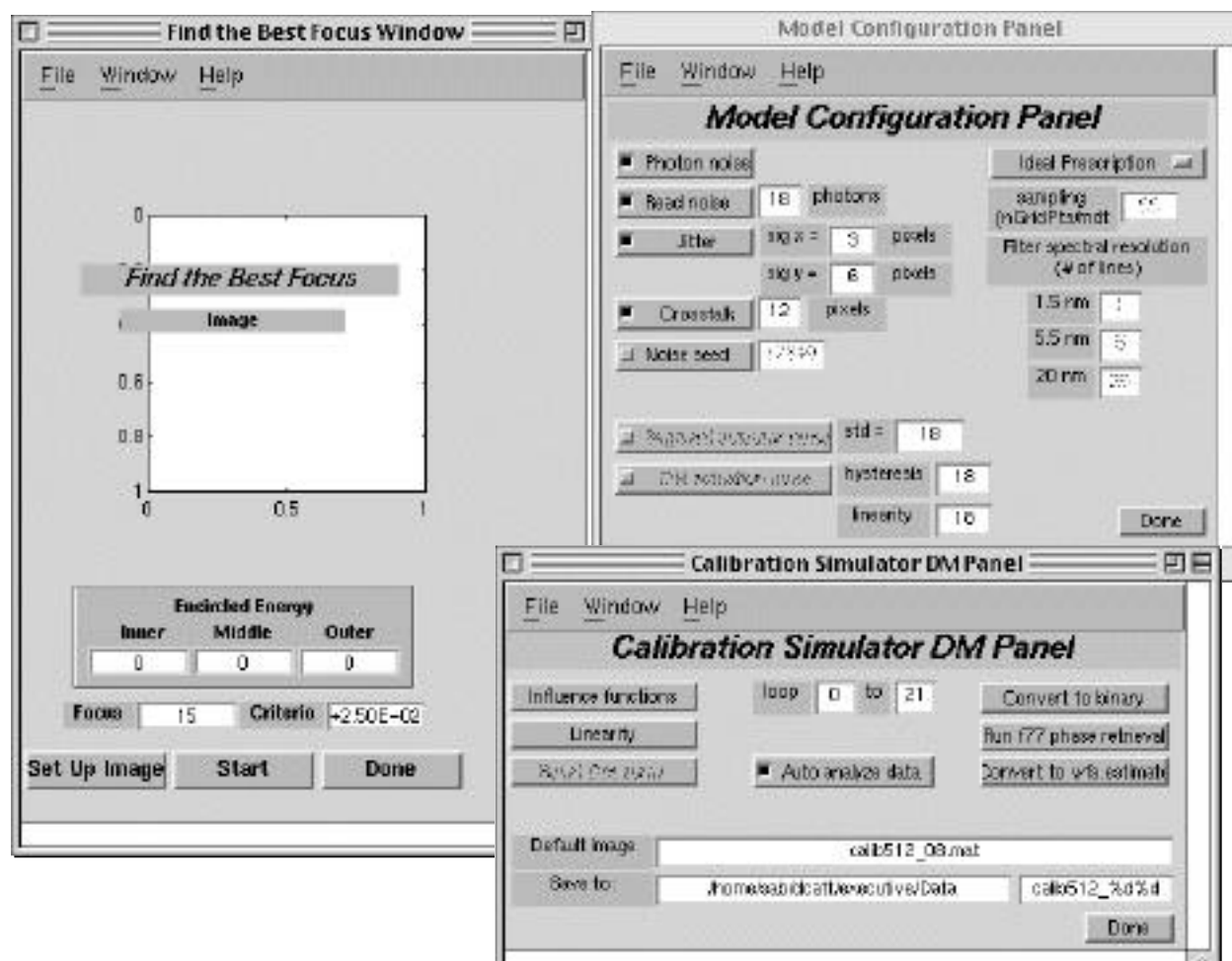

Figure 10. Focus, Simulator DM, and Model Calibration Panels

The WF sensing uses a modified Gerchberg-Saxton iterative-transform phase retrieval algorithm processing focus- (and wavelength-) diverse images to estimate the phase at the exit pupil, as described in Refs. 8 and 9. It works by mixing the intensity data at the focal and pupil planes with model-based phase estimates, as indicated on the flow chart of Fig. 12. Typically 4 focal images and 1 pupil image are used. The focal images are deliberately defocussed, to expose the structure that is the signature of pupil phase irregularities. By defocussing different amounts for each image, the data contains enough diversity to resolve ambiguities. The pupil image defines the illumination and obscuration profiles at the pupil -- an important constraint in the algorithm.

The iteration starts with a random guess at the phase of the pupil used to form one of the images. This starting-guess phase is Fourier transformed to the image plane. The resulting phase is combined with the square-root of the amplitude of the image data to create an estimate of the complex amplitude of the field at the image plane. This is inverse Fourier transformed back to pupil space, where the amplitude is replaced by that determined from the pupil image. The result is an estimate of the complex field at the pupil. This is Fourier transformed back to the image plane, and the process repeats.

This single-image iteration is run 10 or so times for each image, and then the pupil phase estimates (with the diversity phase removed) are combined. The resulting joint estimate of the pupil is then used to start another round of single-image iterations. When changes in the estimated pupil are small from iteration to iteration the process has converged. The WF estimate is the weighted average of the pupil phases.
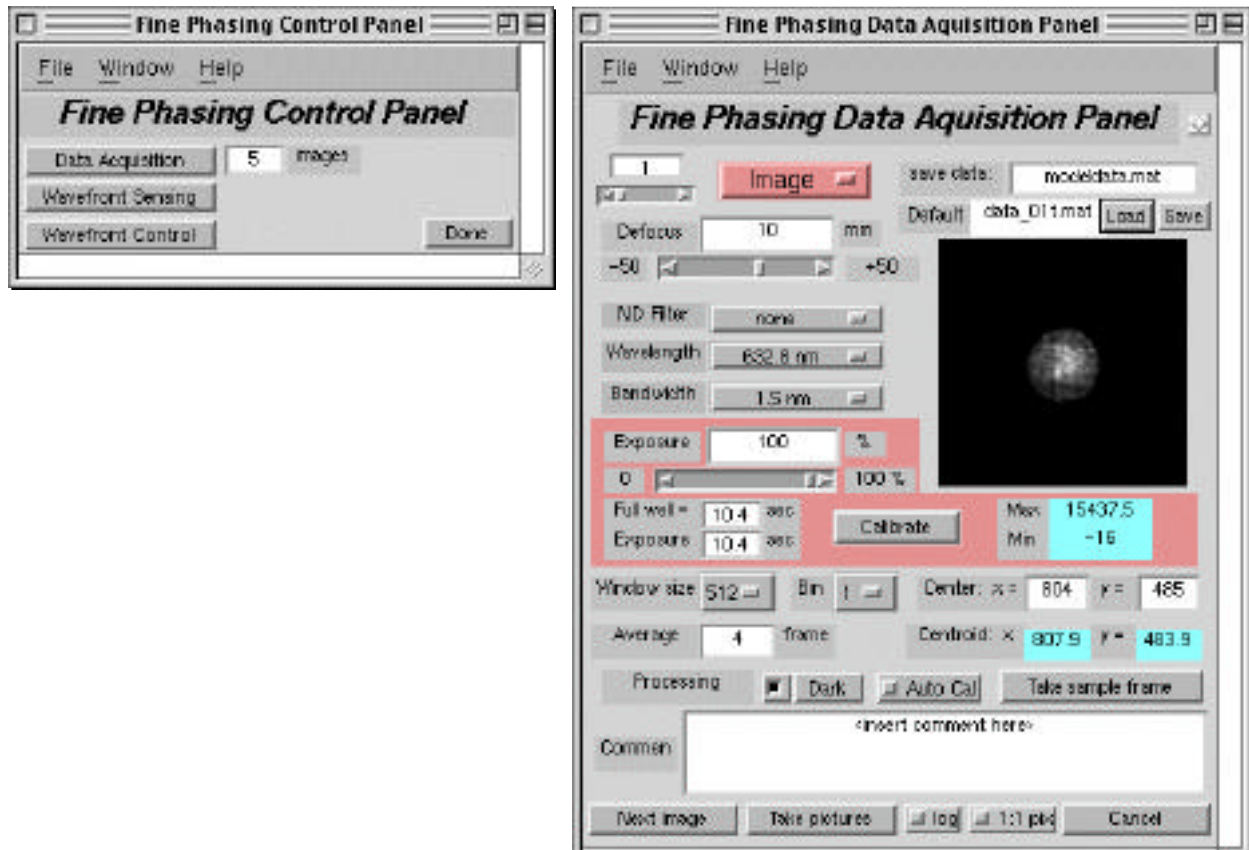
8

Figure 11. Fine Phasing Control and Data Acquisition Panels
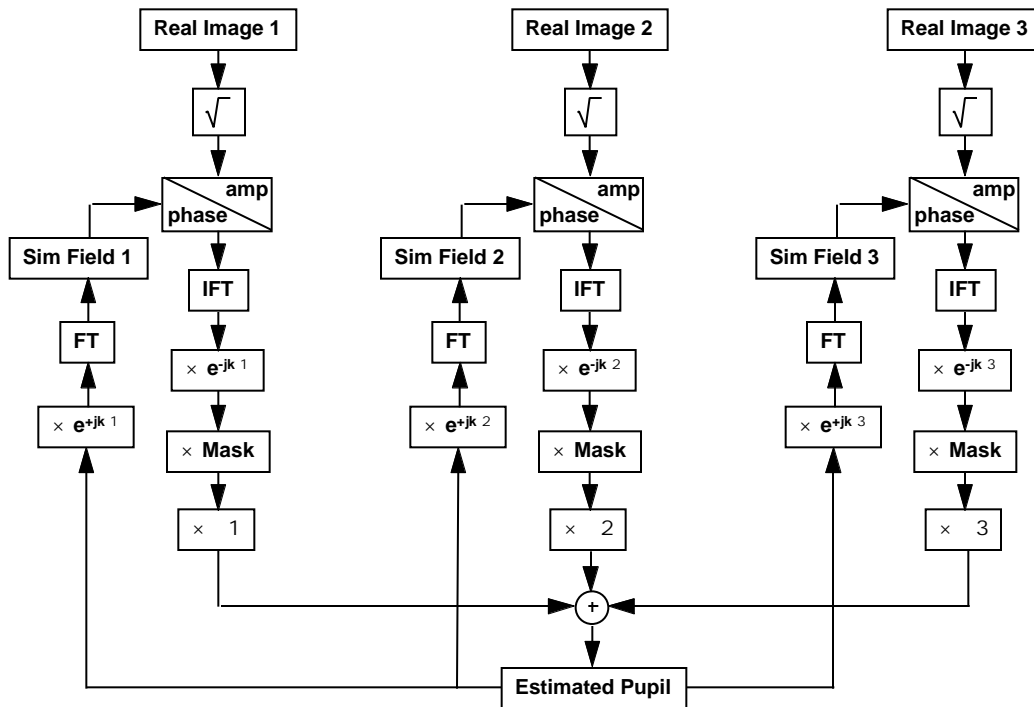

Figure 12. Phase retrieval algorithm

These images are specified individually and in turn using the Data Acquisition panel (Fig. 11). The user first interactively sets all parameters for the first image: whether a focal or pupil image; filter setting (wavelength, bandpass, ND); integration time; defocus; number of frames to be integrated. Then the user clicks on the "next image" button, or moves the image number slider, and the panel is reset for the next image. To check that the various settings are correct, the user can click the "Take Sample Frame" button, and a single frame will be taken and displayed in the window. When all images have been specified, the user clicks the"take pictures" button and the final images are taken.

Most of the results in this report were generated using 4 focal images, at defocus settings of -25 mm, -12.5 mm, 12.5 mm and 25 mm. A pupil image is also used to generate good constraints for the phase retrieval iteration. Other combinations can be successful as well.

Once the data hasbeen taken, the computer stores the data and returns the userto the Fine Phasing panel. The user then selects WF Sensing, which leads to the panel illustrated in Fig. 13.
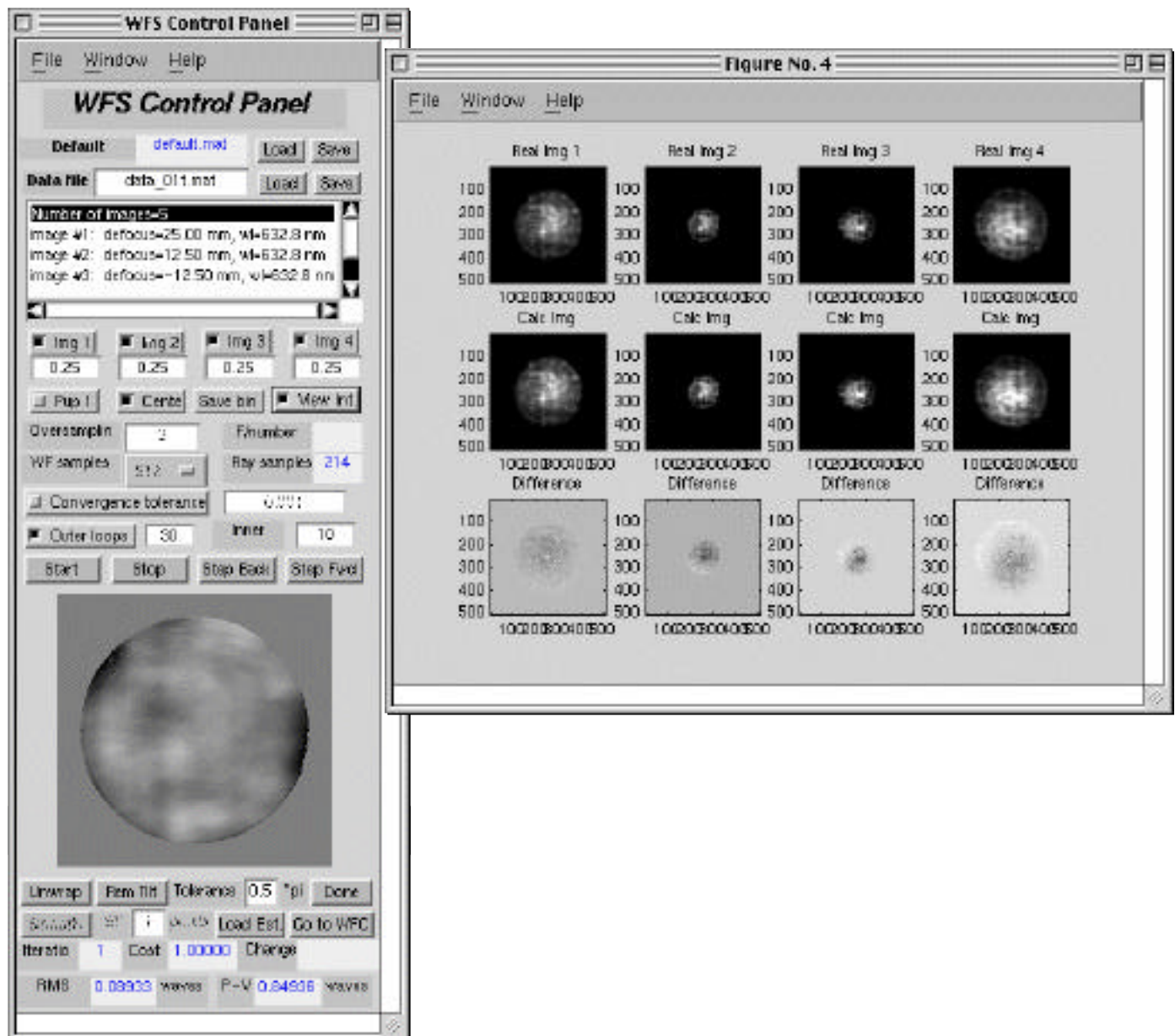

Figure 13. Wavefront Sensing Panel and auxiliary window showing phase retrieval progress

10

The WF Sensing panel is used to set parameters for the phase retrieval, such as the number of images and their relative weight, convergence criteria, and others. When configured as desired, the user can push the "Start" button. An auxiliary window pops up (if "View int." is selected), which is continuously updated during the phase retrieval process. It shows the data images along the top row; current estimated images along the middle row; and the difference along the bottom row. Figure 13 shows the auxiliary window after the WF estimate has converged. Degree of convergence is estimated by how well the images derived from the estimate match the data images in a ^{2} sense. As shown in Fig. 13, they match the images very closely indeed.

The phase retrieval processing can also be run externally to the Executive, by pushing the "Save bin" and "Run external" buttons. These pass control to an external process that utilizes multiple processors and compiled-language versions of the phase retrieval code to execute much faster than the internal algorithm can. Control is returned to the WF Sensing panel when the external program is done.

The estimated WF of Fig. 13 shows some interesting structure. There are distinct vertical streaks in the WF, due to OAP figure error residuals. There are some bumps and dips, due to differences in DM actuator gains, and a slight astigmatic cast (recall we set the DM to "Half" and "Add astigmatism"). These effects will be compensated by the WF control, which is invoked next by pushing the "Go to WFC" button. This brings up the WF control panel shown in Fig. 14..
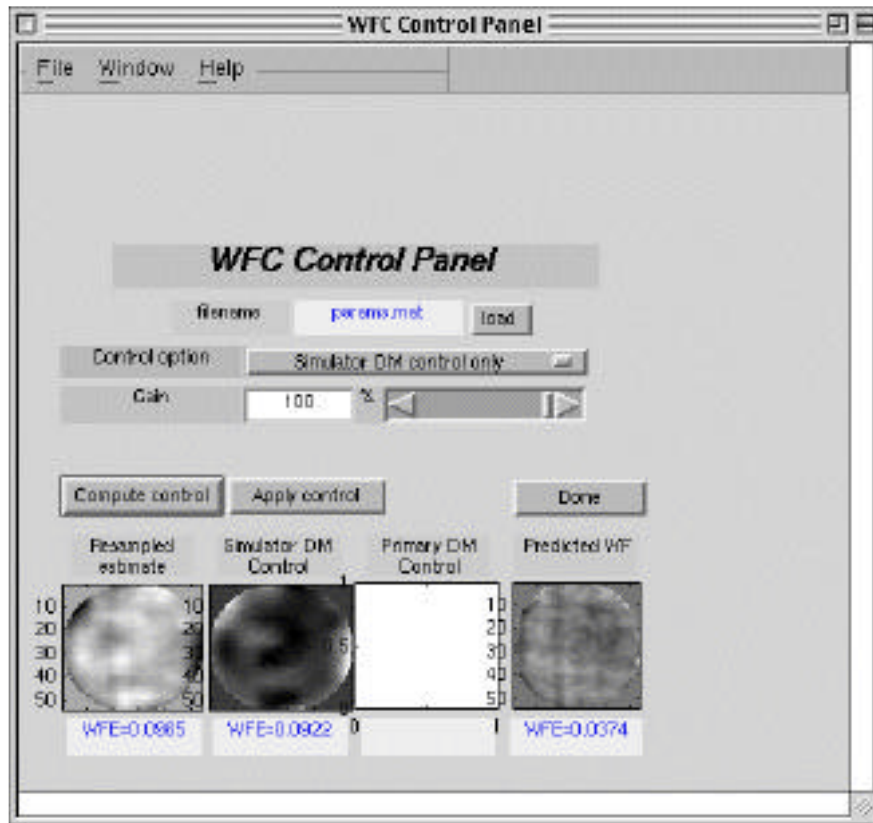

Figure 14. Wavefront Control Panel

The WF Control panel is used to specify the type of control to be applied, to compute the control settings accordingly, and to implement the control. The "control option" pull-down menu allows selection of different control types. In the current configuration, the only choice is to set the simulator DM. With the addition of the AO bench, the AO DM can be set as well. When the telescope is specified, the user is able to select from AO DM control, AO DM and segment control, segment control only, and alignment control (segment decenter and twist). The "Gain" slider allows the user to damp the control inputs, for instance to prevent overshoot. We found that performance improved in successive iterations by slight damping (80 %) after the initial control step.

11

After selecting the preferred control option, the "Compute control" button is pushed, and the control values are computed, but not applied to the hardware. The results of the control are displayed in the "Simulator DM Control" and "Predicted WF" frames, with predicted RMS WFE numbers displayed below. In our example case, the WFE is predicted to decrease from the estimated 0.087 waves to 0.037 waves.

The DM control display shows clearly that the Simulator DM influence functions are wider than some of the structure in the actual WF. This provides a limiting factor to the effectiveness of the SDM control, as this higher spatial-frequency structure is beyond the SDM spatial frequency bandwidth. The AO DM, when installed, will be more effective in correcting these effects.

The user can change control options, or gain value, and repeat the control calculation as many times as desired. The control calculations resample the estimate to the pixel sampling density used for the calibrated DM influence functions, and then solve a simple static optimal control problem to determine new actuator settings that minimize WFE. This approach is described in Refs. 8 and 9.

When the control is as desired, the user can push the "Apply control" button to send the control settings to the hardware, where they are implemented. The WF Control panel is then closed, and the user is returned to the "Init" panel. The user may return to the WF Control panel after applying the control, perhaps to experiment with alternate control options in the "Predicted WF" frame, but be warned -- applying more than 1 set of controls without first taking new WF sensing data will essentially reapply the error, and destroy the correction.

After applying the control, its effectiveness can be determined by repeating the WF sensing process. The user invokes Fine Phasing, takes new data, performs the WF sensing processing. The new WF estimates show the actual effect of the control, and typically match the Predicted WF well. There are some small differences expected, due to DM actuator errors, WF sensing errors, and DM influence function errors. In what follows, we report on some experiments designed to determine the magnitude of these effects.

4. Wavefront sensing results

4.1 Comparing Zygo and WFS measurements

It is highly desirable to have an independent check of the accuracy of the WFsensing results. With this in mind, we made independent measurements of the Simulator WF using a Zygo interferometer in double pass. This provided a less than perfect check, however, for 3 reasons.

The first is that the Zygo follows a slightly different optical path within the Simulator, as it goes through the DCATT beamsplitter 2 times, while the Source illumination is reflected once and transmitted once by the same beamsplitter. This was calculated to introduce about 0.04 waves of astigmatism into the Zygo measurement -- an error that is not in the WF sensor measurement.

A second source of non-common path error is due to the Zygo transmission sphere. The transmission sphere, located at the output of the interferometer, acts to focus the interferometer beam into the test article and, in reflection, to provide the interference reference beam as well. Aberrations in the transmission sphere directly contribute errors into the Zygo measurements. The manufacturer's test report for the reference sphere is shown in Fig. 15, which indicates that an error of 0.014 waves RMS and 0.077 waves peak-to-valley can be expected. This effect is complicated by the fact that the alignment of the reference sphere was not well controlled in the measurements we made, so the precise location of these effects in our wavefronts is not known.

A third source of error was contributed by jitter of the interferometer. The temporary mounting we usedto attach and align the interferometer to the optical bench was perhaps too flimsy. In any event, it was quite difficult to get adequate fringes, with 4 out of 5 attempts having too many dropouts to be useful. Frame-to-frame repeatability showed significant variations, with the astigmatism term alone varying by as much as 0.04 waves between successive frames.
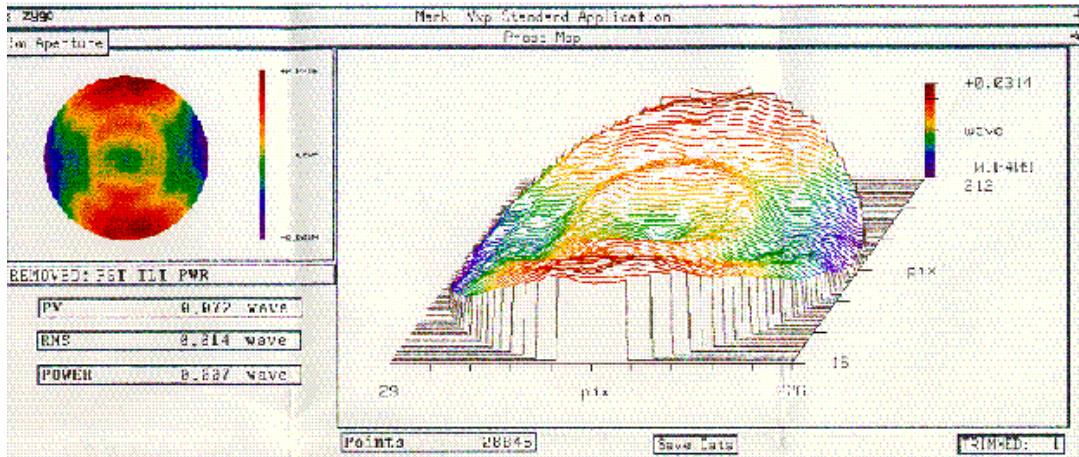
Figure 15. Zygo transmission sphere aberrations

To make the comparison between the WFS and the Zygo, we first ran the WFS through the entire sensing procedure. This was done for 2 cases: with the unpowered DM; and with the return mirror in place of the DM. Then we removed the WF sensor camera and used the Zygo to measure wavefronts in the same configurations. The location of the Zygo can be seen in Fig. 1; it is the blue object at the lower right. The WFS and Zygo results were compared by resampling to a common dimension, removing tilt and power, and subtracting the Zygo from the WFS results. The resulting WFs are shown in Figs. 16 and 17.

Retrieved phase, SSC with DM	Zygo phase, SSC with DM	Retrieved - Zygo phase
PV=277, RMS=42nm	PV=352, RMS=41nm	PV=275, RMS=38nm
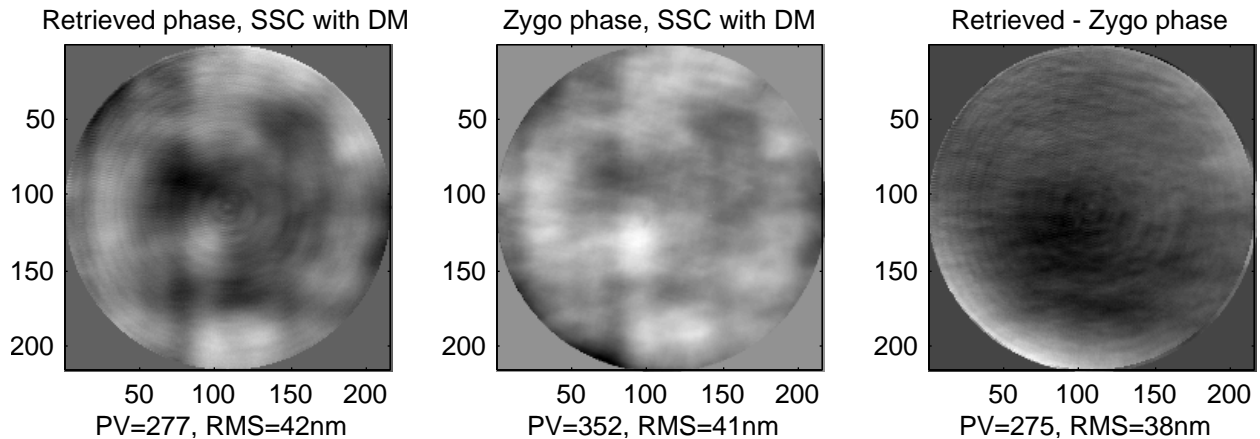
Figure 16. Comparing Zygo and WFS measurements, deformable mirror in place

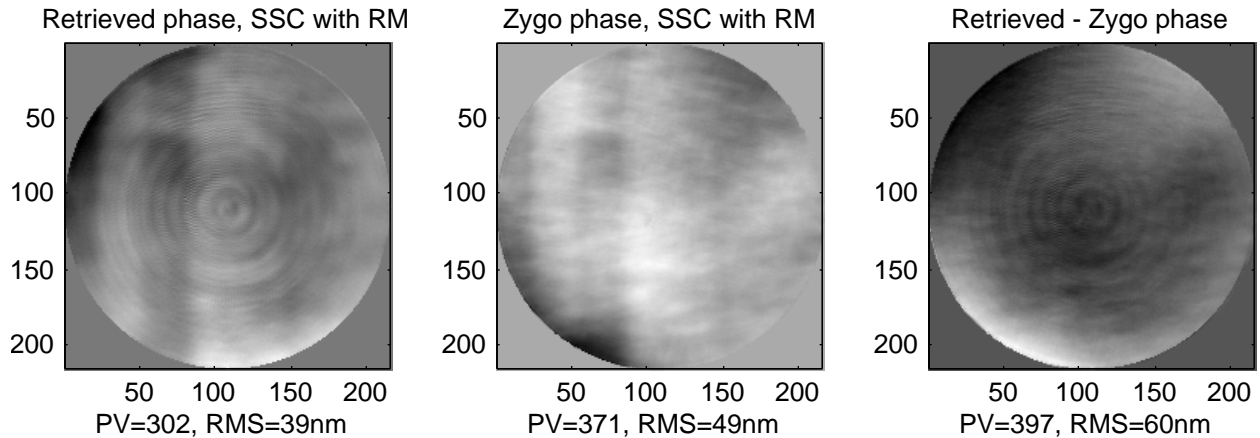| Retrieved phase, SSC with RM	Zygo phase, SSC with RM	Retrieved - Zygo phase
PV=302, RMS=39nm	PV=371, RMS=49nm	PV=397, RMS=60nm

Figure 17. Comparing Zygo and WFS measurements, return mirror in place

13

The Zygo and WFS results are consistent in some respects and show differences in others. For both the DM and RM cases, the high spatial-frequency structure is very nearly the same. The OAP gouges and the DM bumps are consistent between the 2 measurement techniques, and are removed in the subtracted frames. In both cases, the Zygo estimates shows a significant bulge in the lower center region, and a smooth, mostly astigmatic residual error, compared to the WFS estimates. These differences are at the 0.04 waves level, consistent with the 0.04 waves of repeatability error, and the 0.04 waves of beamsplitter and 0.014 waves of transmission sphere noncommon path error. Qualitatively, the bulge is consistent with the bulge seen in the transmission sphere aberrations (Fig. 15).

Overall, the WFS and Zygo results are comparable, within the error bar expected for the Zygo measurements. Better Zygo measurements will be made at GSFC, when the Source, Simulator and WFS are integrated with the AO bench. The AO bench beamsplitter is expected to have significantly less difference between the transmitted and reflected paths, and care will be taken to better mount the Zygo. It is also clear that the Zygo should be carefully calibrated to determine the precise contribution of the GSFC transmission sphere to the Zygo WF measurements. If this is done, the Zygo measurements should provide a useful check on the WFS.

Longer term, we are planning to build a multi-color Interferometric WFS (IWFS) for scoring the WFS when it is integrated with the telescope. The IWFS will run in single-pass mode to reduce long-path seeing errors and noncommon path errors. Its multi-color capability is required to resolve absolute piston errors between segments. The latter, especially, is an important capability not provided by commercial interferometers. The IWFS will have a synthetic equivalent testing wavelength of more than 20 um.

4.2   WFS repeatability

Experiments were run to determine consistency between different WFS measurements of the same wavefront. These provide data on the total WFS error, combining effects of detection noise, residual stray light, jitter, bandpass blurring, lab seeing, etc. They do not expose any systematic error, such as modeling error in the phase retrievals. Systematic errors are expected to be quite small, because the optical path and the detector are the same for the WFS as for the science camera, and because careful calibration is done to ensure that the models agree precisely with the hardware.

The first repeatability test began by flattening the wavefront with 2 successive cycles of Fine Phasing control. The result was a wavefront with WFE of λ/36.5, or 17.3 nm, and peak-to-valley of λ/3.67, or 172 nm. The DM was left in this configuration, and a series of 10 more estimates was made, using the Fine Phasing Data Acquisition and WF Sensing panels. The white light source together with the 3 nm-wide 632.8 nm wavelength filter was used in each case. Four image frames were averaged for each image, with dark frame subtraction. Pupil images were used in the phase retrieval calculations.

The retrieved estimates are shown in Fig. 18, and the average of all 10 estimates is shown in Fig. 19. Also shown in Fig. 19 is the pixel-by-pixel standard deviation for all 10 frames. The individual estimates are, to the eye, essentially identical. An exception is an area of occaisionally noisy pixels in the lower-left quadrant. The noisy area shows up vividly in the standard deviation frame. It is smoothed out in the average frame.

Each estimate (and the average frame) shows the same residual high-frequency aberrations that were apparent after the first experiment described earlier: vertical stripes due to residual OAP figure error; some other dips where the wide SDM actuators do not exactly smooth DM or other optical figure errors; and a dip in the upper left corner of the pupil. The latter is due to the single dead actuator of the SDM, which, although out of the clear aperture, exerts some influence on the edge of the mirror. Still, the residual "figure" error, if ascribed wholly to the DM, is λ/73 at λ=632.8 nm, well below the basic DCATT requirement of λ/20 at a wavelength of 2000 nm. The estimates also show some low-level artifacts of the phase retrieval process, chiefly a highly regular cyclic ringing. This effect is seen in retrievals against model-generated data as well; it is reduced by increasing zero padding in the phaseretrieval FFTs.

After determining the average frame, difference frames were generated for each individual estimate, by subtracting the average frame. The results are shown in Fig. 20. The average RMS value for the difference

frames is λ/115 at 632.8 nm, or 5.5 nm. This represents the frame-to-frame WFS error for a nearly flat WF.
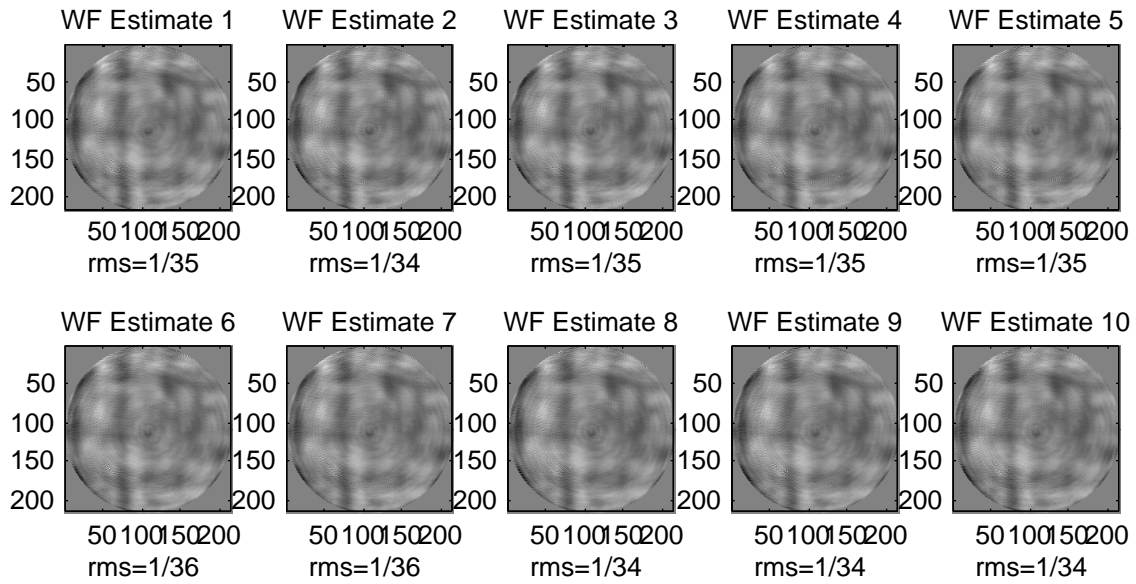
WF Estimate 1   WF Estimate 2   WF Estimate 3   WF Estimate 4   WF Estimate 5

rms=1/35   rms=1/34   rms=1/35   rms=1/35   rms=1/35

WF Estimate 6   WF Estimate 7   WF Estimate 8   WF Estimate 9   WF Estimate 10

rms=1/36   rms=1/36   rms=1/34   rms=1/34   rms=1/34

Figure 18. Ten sequential WF estimates, flattened DM (tilt removed)

Mean WF Estimate   WF Estimate Std Dev
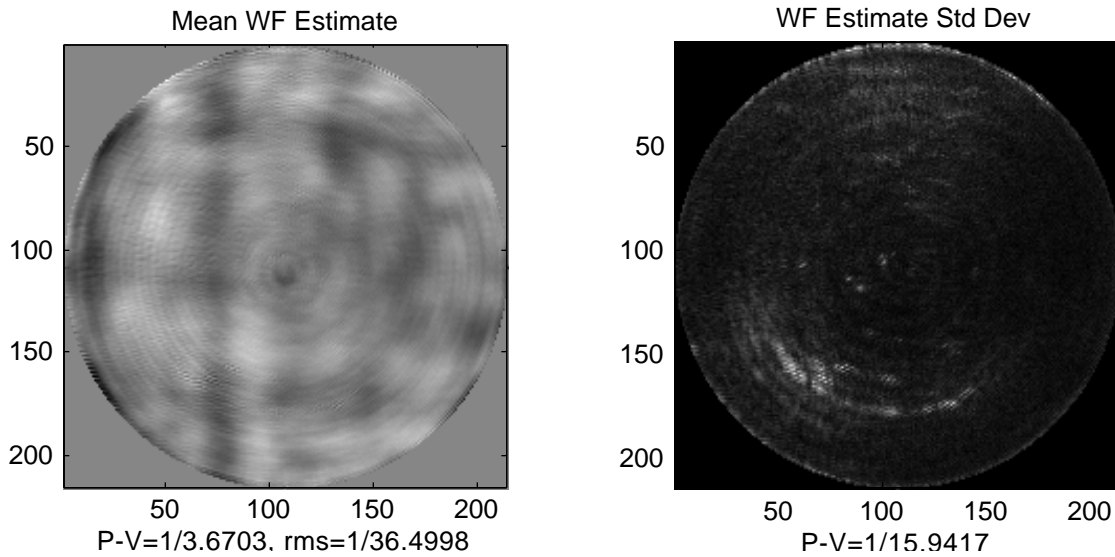

P-V=1/3.6703, rms=1/36.4998   P-V=1/15.9417

Figure 19. Average and standard deviation of 10 WF estimates, flattened DM (RMS of the standard deviation frame is λ/240).

Est 1 - Avg	Est 2 - Avg	Est 3 - Avg	Est 4 - Avg	Est 5 - Avg
RMS=1/116	RMS=1/112	RMS=1/116	RMS=1/119	RMS=1/115

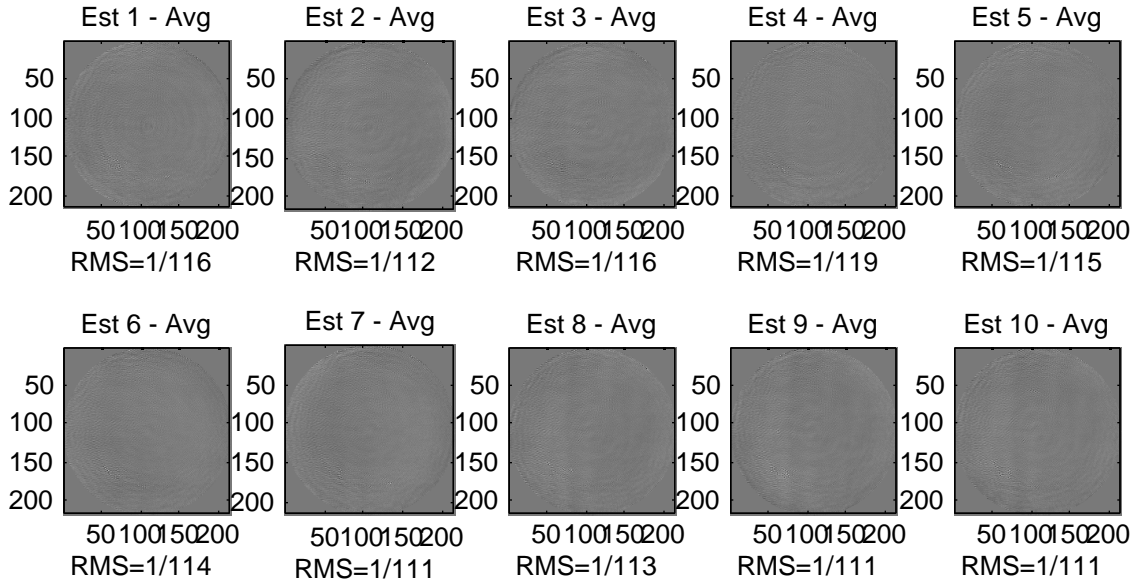| Est 6 - Avg	Est 7 - Avg	Est 8 - Avg	Est 9 - Avg	Est 10 - Avg
RMS=1/114	RMS=1/111	RMS=1/113	RMS=1/111	RMS=1/111

Figure 20. Estimates minus the average of the estimates, fl   attened DM

The next repeatability test was run for a slightly aberrated WF, created by pushing up a single actuator. The resuting WF error was   /13. As before, the white light source was used with the 3 nm-wide 632.8 nm wavelength filter. Four image frames were averaged for each image, with dark frame subtraction. Pupil images were used in the phase retrieval calculations.

The resulting estimates are shown in Fig. 21, the average and standard deviation frames are in Fig. 22, and the mean-subtracted frames are in Fig. 23. The estimates show a region of noisy pixels, except here it is more concentrated and higher amplitude than with the flat WF. The level of noise seen in this test was greater than we observed in any others; exactly why it occurred will be studied. Nonetheless, the WFS noise in this case was only   /92.
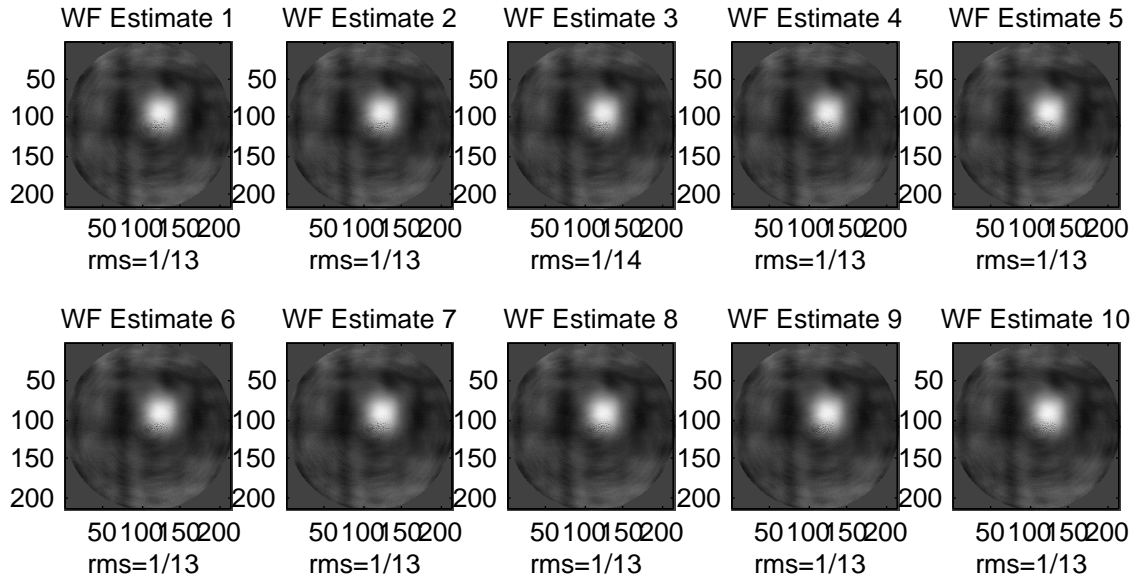

WF Estimate 1	WF Estimate 2	WF Estimate 3	WF Estimate 4	WF Estimate 5
rms=1/13	rms=1/13	rms=1/14	rms=1/13	rms=1/13

WF Estimate 6	WF Estimate 7	WF Estimate 8	WF Estimate 9	WF Estimate 10
rms=1/13	rms=1/13	rms=1/13	rms=1/13	rms=1/13

Figure 21. Ten sequential WF estimates, single actuator poked (tilt removed)

16

Mean WF Estimate

WF Estimate Std Dev

P-V=1/1.7896, rms=1/13.5812

P-V=1/5.6279, rms=1/140.3652
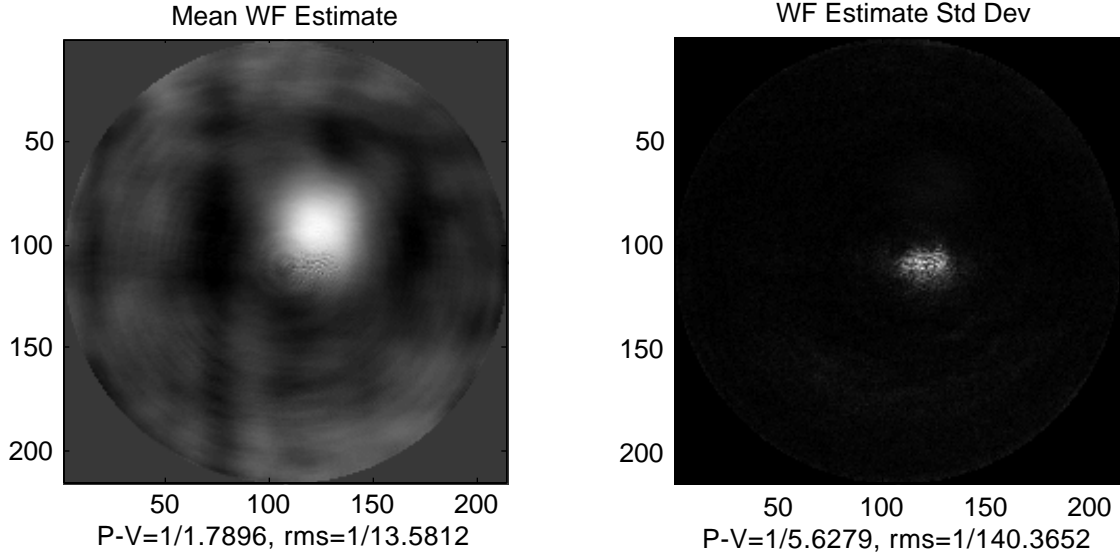
Figure 22. Average and standard deviation of 10 WF estimates, single actuator poked

Est 1 - Avg

Est 2 - Avg

Est 3 - Avg

Est 4 - Avg

Est 5 - Avg

RMS=1/87

RMS=1/90

RMS=1/84

RMS=1/91

RMS=1/93

Est 6 - Avg

Est 7 - Avg

Est 8 - Avg

Est 9 - Avg

Est 10 - Avg

RMS=1/95

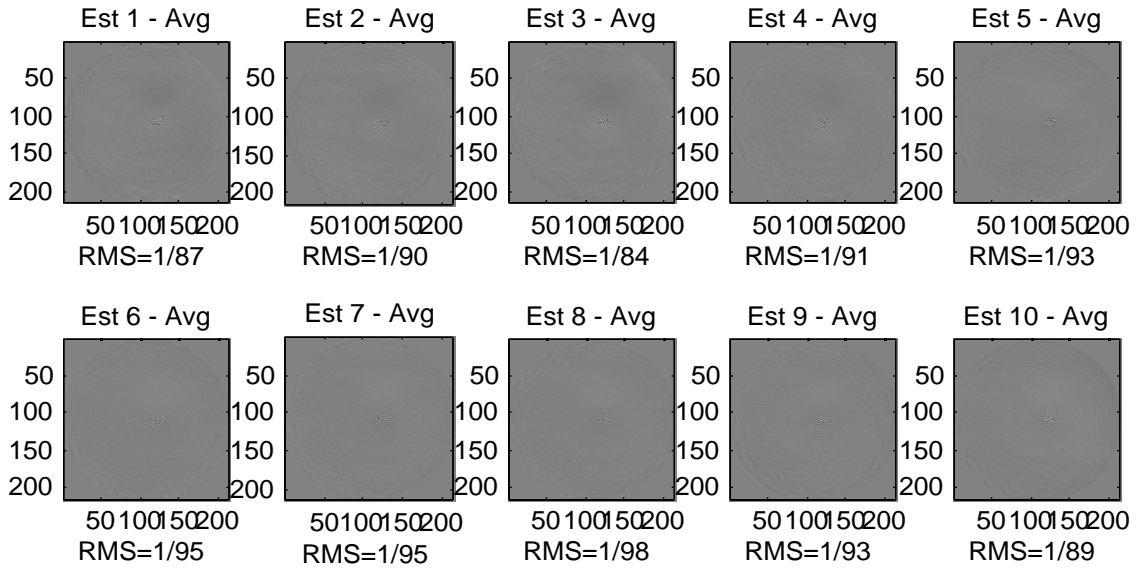RMS=1/95

RMS=1/98

RMS=1/93

RMS=1/89

Figure 23. Estimates minus the average of the estimates, actuator poked

The third repeatability test was run for a different aberrated WF, generated in much the same way as the detailed example discussed earlier, by starting with the DM at the half-way point and adding astigmatism. The resulting WF error was /12. The white light source was used with the 3 nm-wide 632.8 nm wavelength filter. Four image frames were averaged for each image, with dark frame subtraction. Pupil images were used in the phase retrieval calculations.

The resulting estimates are shown in Fig. 24, the average and standard deviation frames are in Fig. 25, and the mean-subtracted frames are in Fig. 26. The estimates also show a region of noisy pixels, now located in the upper left. The average WFS noise in this case was /104.
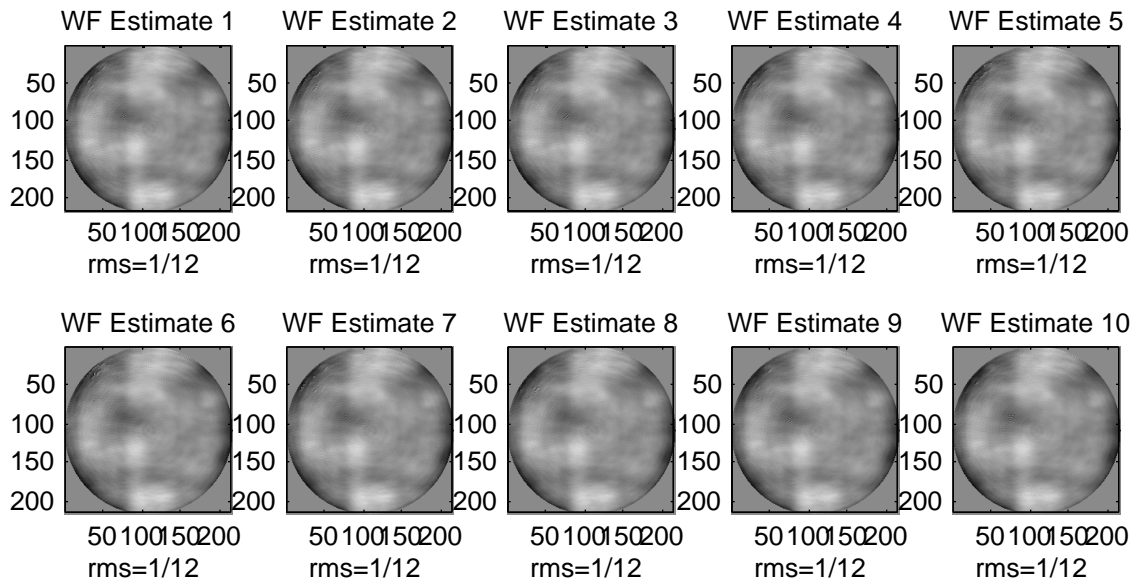
17

Figure 24. Ten sequential WF estimates, DM "astigmatism" setting (tilt removed)
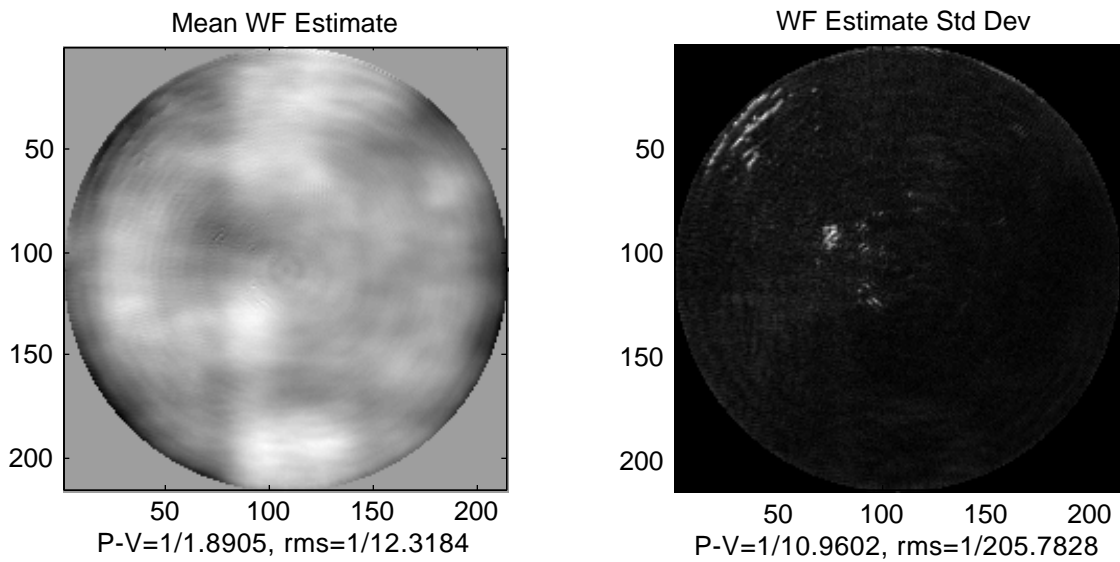

Figure 25. Average and standard deviation of 10 WF estimates, DM "astigmatism" setting
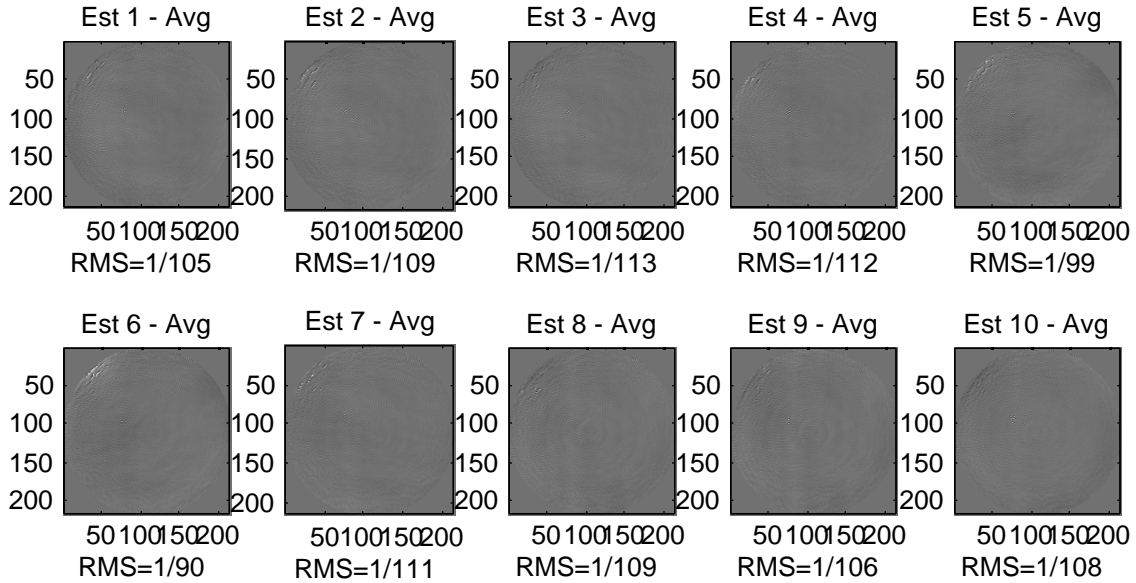
Figure 26. Estimates minus the average of the estimates, DM "astigmatism" setting

4.3   Effect of spectral bandpass

The phase retrieval algorithm of Fig. 12 assumes the use of monochromatic light. If instead the illumination has a finite spectral band, then the PSF-to-pupil transformation model used in the algorithm is no longer fully correct. The actual PSF is spectrally "blurred," and the transformation from the data to pupil phase is also somewhat blurred. The result is some error in the WF sensing process.

On the other hand,a wider bandpass allows more light through the system, so that image integration times can be significantly shorter. There is a trade-off to be made between WFS accuracy and imaging time.

The tests described in this section explore the amount of WF sensing error contributed by using the DCATT bandwidth filters, which provide 3 nm, 11 nm and 40 nm bandwidth illumination at 632.8 nm wavelength. Five images were taken using the 11 nm filter, and 3 using the 40 nm filter, with the DM in the "poked actuator" configuration of the previous section. These were processed using the WF Sensing panel and then averaged. The averaged estimates are shown in Fig. 27. There they are compared to the average frame generated from 10 separate estimates taken using the 3 nm filter.

Note that the noisy pixels of the previous section are not seen in the 3 nm data. The data in this section was taken earlier, using a slightly different alignment of the optics and a 30 nm pinhole instead of the 25 nm pinhole used in the repeatability test.

There is little apparent difference between the WF estimates. All show the same characteristics -- the OAP gouges, the DM bumps, the single pokedactuator. The differences are more apparent when looking at the difference frames of the wavefronts (also shown in Fig. 27). These show a slight, low-order aberration between the narrow bandpass estimate and the 2 others. The magnitude of this difference is about $\lambda/30$. It is unclear, however, that it is a consequence of the different bandpasses. It looks too much like an alignment shift to allow confidence that it is due to the bandpass effect.

This test does show that penalties for using the wider filters are not severe, but further experimentation is required to pin down the real magnitude of this effect.
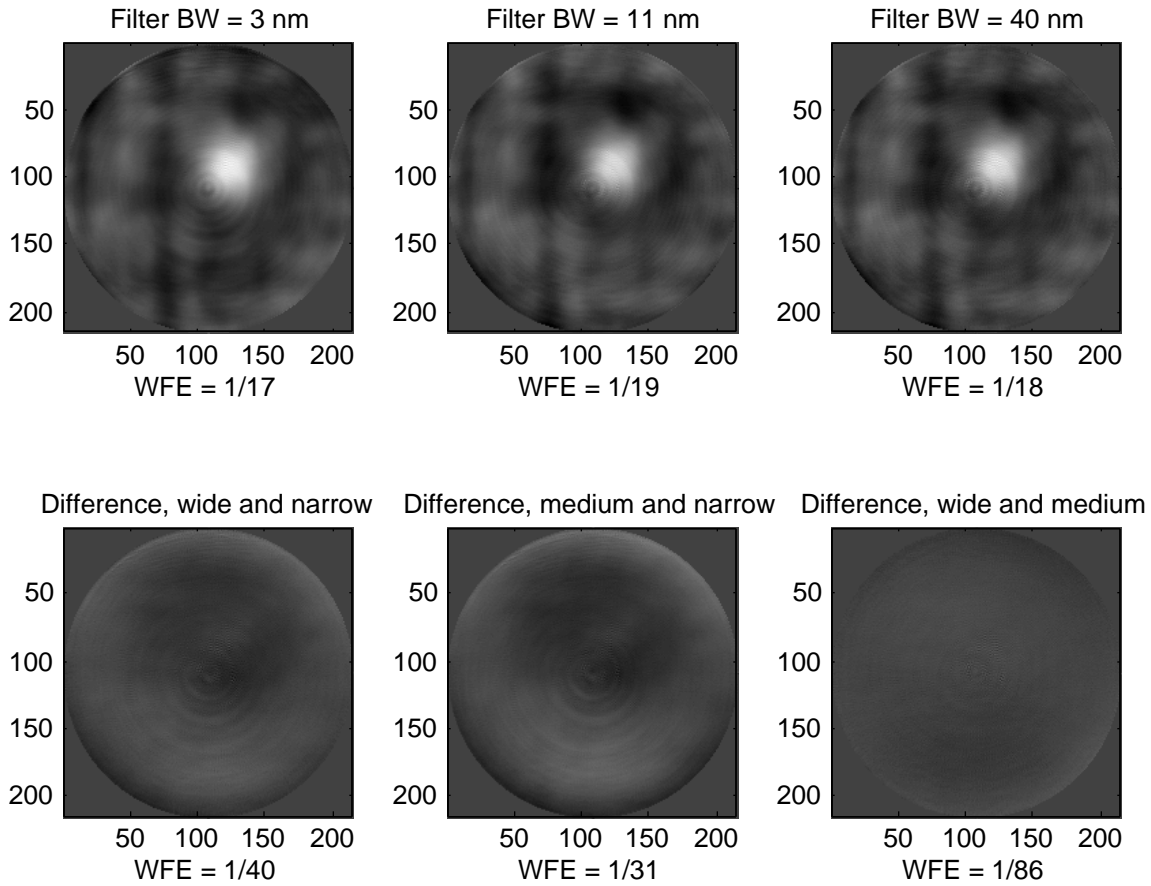
19

Filter BW = 3 nm	Filter BW = 11 nm	Filter BW = 40 nm

WFE = 1/17	WFE = 1/19	WFE = 1/18

Difference, wide and narrow	Difference, medium and narrow	Difference, wide and medium

WFE = 1/40	WFE = 1/31	WFE = 1/86

Figure 27. WF Estimates taken at 3 dif   ferent bandpasses,   = 632.8 nm

4.4   Effect of wavelength

Wavefront sensing using multiple wavelengths of light, through selection of different wavelength filters, is essential in resolving the true relative piston of the NGST and DCATT primary mirror segments. In the Coarse Phasing control, relatively wide bandpass filters are used, together with a grism to create a dispersed-fringe phase sensor, or in a piston scanning mode, to determine the relative piston of 2 segments over a large dynamic range (Ref. 8).

In Fine Phasing control, multiple wavelengths can be used for the same reason, but without the same dynamic range requirement, since Fine Phasing will usually be conducted when the segments are already phased to within a wave. By combining multiple retrievals of slightly different wavelength narrow-band filters to generate a long synthetic wavelength, they allow determination of relative piston over a range much greater than the wavelength of the illumination. For the filters provided in the Source, this range is greater than 20 um. Multiple colors can also be of use in the WFS processing, where they can help in unwrapping phase estimates, and in providing data diversity.

Only very limited testing has been done to date at wavelengths other than 632.8 nm. This area will be pursued more actively when the DCATT telescope is integrated. For now, only 2 WF estimates have been made at other than 632.8 nm. These were made at 514 nm and 795 nm, with the DM flattened, and are shown in Fig. 28.

The different estimates taken at the 3 different wavelengths agree within 6.4 nm WFE. Some structural differences are noted between the estimate taken at 795 nm. These may be due to modeling inconsistencies in the WFS processing.
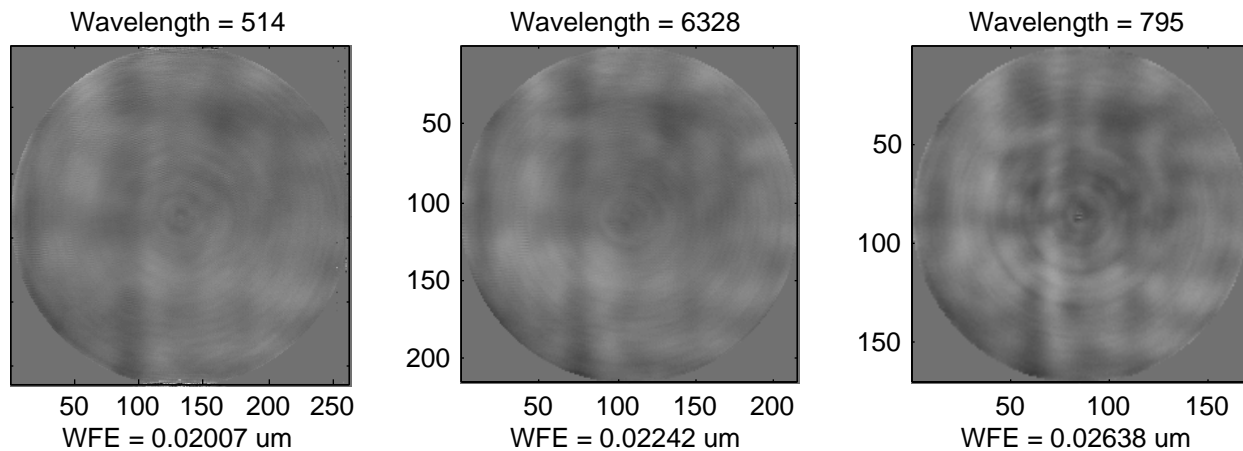
Wavelength = 514	Wavelength = 6328	Wavelength = 795
WFE = 0.02007 um	WFE = 0.02242 um	WFE = 0.02638 um

Figure 28. WF estimates taken at 3 dif ferent wavelengths

4.5   Other WF sensing issues

Some limited testing was performed to check functionality of the WF sensing in other modes and conditions:

1. Pupil illumination profile. Retrievals were performed in all the pinhole configurationsdescribed earlier. All converged nicely and produced estimates that agree with those shown here.

2. Laser illumination. The laser wasused with excellent results, producing WF estimates that agree with those shown here.

3. Camera dynamic range. Data was collected using shorter exposures and fewer integrated frames. These images had less overall dynamic range. They were processed successfully, showing some small degradation compared with those run to full well and averaged over multiple exposures. More thorough experiments will be conducted and reported later.

5.   Jitter

Image jitter, or vibration, has at least 2 causes. The first is mechanical vibration of the optics, source or sensor on the optical bench. The second is atmospheric turbulence, or "lab seeing." The effect of jitter is to blur the images used for WFS processing, potentially introducing WFS error. Monte Carlo analyses indicate that levels of jitter below about a half of a pixel lead to errors smaller than   ∕100.

Some limited testing was performed to determine combined jitter levels. Two sequences of short-exposure images were taken andanalyzed for total image motion. The first sequence was run before the covers and baffles were installed, while the optics were fully exposed to the lab environment (Figs. 4 and 7). The second was taken after the source and simulator were fully enclosed, greatly reducing the exposure of the optics to turbulence. The laser was used in both cases.

In the first test in-focus images were used. Exposure times were set at the minimum that the camera shutter supports, 0.1 sec. The images are shown in Fig. 29. Careful inspection shows only quite small variations from image to image. Each frame was centroided, with the results plotted in Fig. 30. Peak-to-valley jitter was 0.25 pixels, with an RMS in X and Y of less than 0.06 pixels.

The second test used slightly defocussed images, to improve the accuracy of the centroiding calculations. Exposure time was 0.1 sec as for the first test. The images are shown in Fig. 31, and centroid motion is plotted in Fig. 32. Again, differences from frame to frame are very small. The centroid motion was about 0.1 pixels peak-to-valley and less than 0.04 pixels RMS.

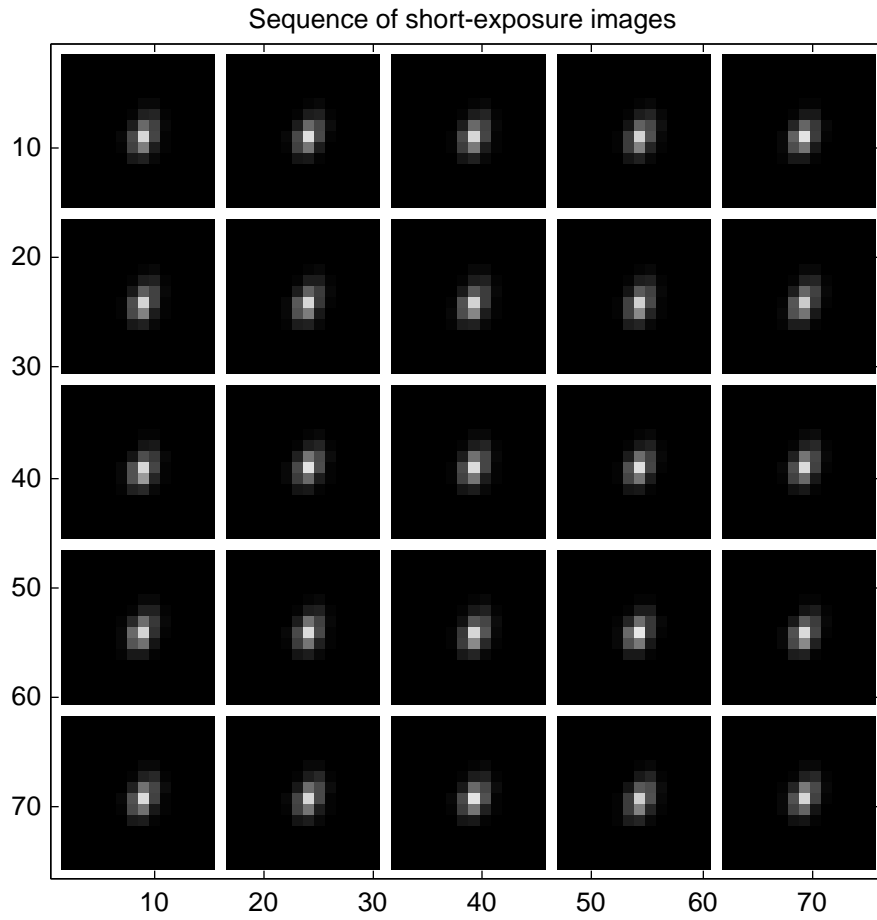This level of jitter is well below that required for DCATT.

Sequence of short-exposure images

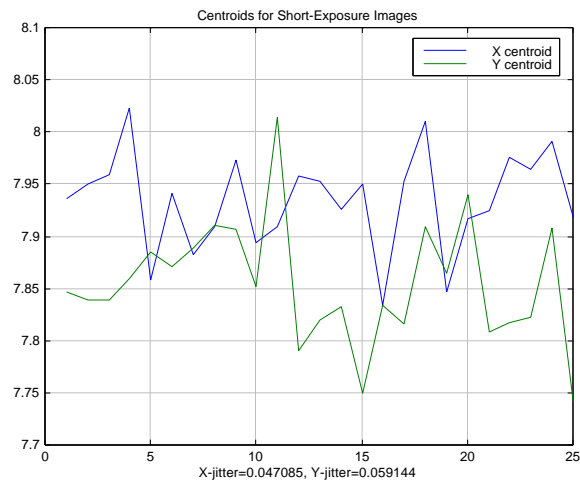**Figure 29. Sequence of short-exposure in-focus images (open optics)**

Figure 30. Jitter results: open source and simulator optics
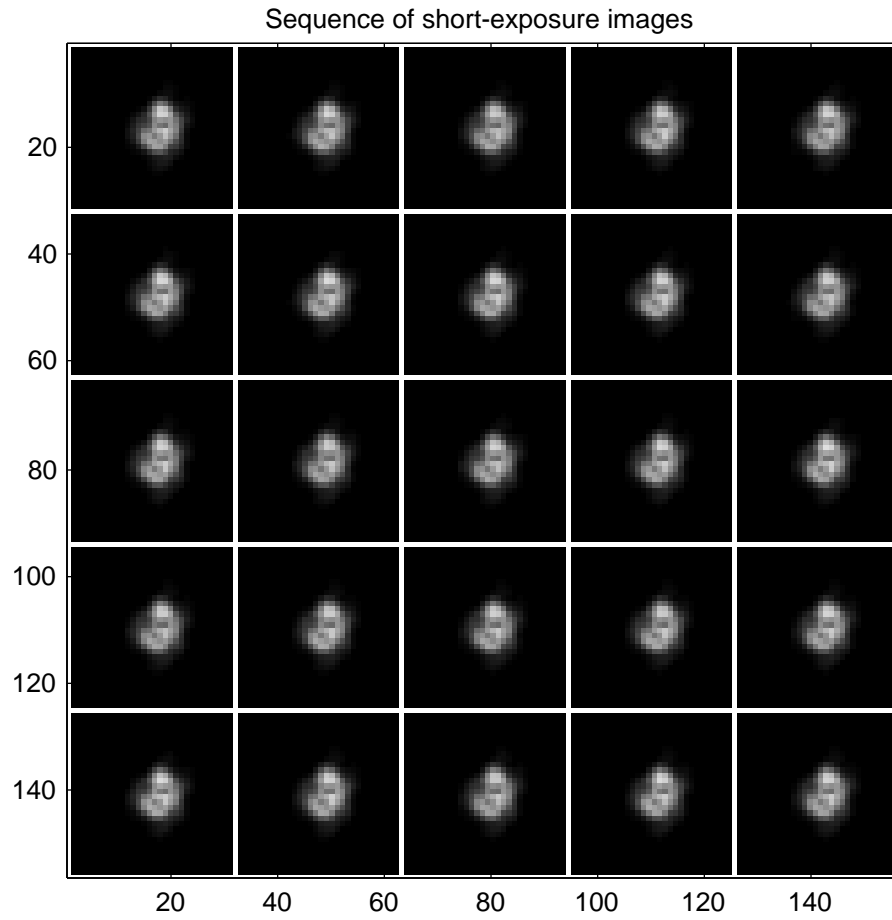
Sequence of short-exposure images

Figure 31. Sequence of short-exposure defocussed images (enclosed optics)

Centroids for Short-Exposure Images
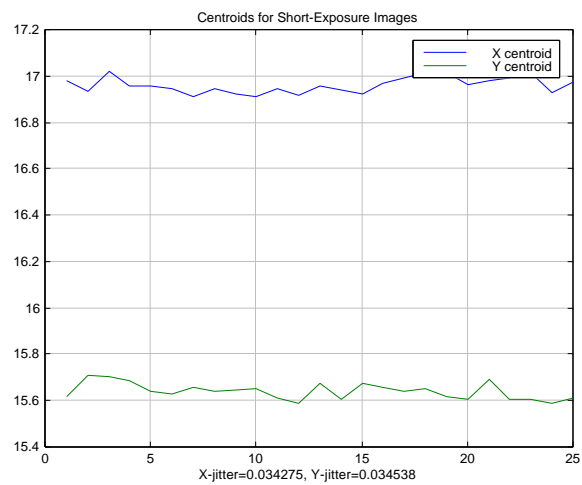
X-jitter=0.034275, Y-jitter=0.034538

Figure 32. Jitter results: enclosed source and simulator

6.   Deformable mirror performance

Testing of the Simulator DM was performed for a couple of purposes. First, it was necessary to determine the influence functions of the actuators, that is, the effectonthe wavefront of a unit poke of each actuatorindividually. This data is combined into a large matrix giving the sensitivity of the WF to all of the DM actuators. This matrix is then used to determine the control gain matrix, which transforms a wavefront into the set of actuator commands that minimize the wavefront errors.

The second objective was to measure the linearity andhysterisis errors expected from this mirror. These errors set a noise floor for the entire WF control process. Of course, ultimate DCATT performance willbe set by the errors in the AO bench DM rather than the Simulator DM -- the latter is ultimately intended to be used as an aberrator rather than a control device.

We tested 2 approaches to determining influence functions. The first poked actuators in 4-actuator patterns, choosing actuators separated by 4 actuator locations in y and 5 in x. The separation of the tested actuators was judged too small, however, after we had difficulties in decoupling influence functions. The second approach was simply to poke each actuator individually. A typical example is shown in Fig. 33. In all 52 actuators were measured, not all of which are within the DM clear aperture. As shown in Fig. 33, the influence of an individual actuator extends out 2 or 3 actuator spacings, so all actuators within that radius of the clear aperture were measured.

After theactuators were measured they were down-sampledto the control sampling density of 55 pixels/aperture (Fig. 34). This sampling was chosen as it over-resolves the individual actuators yet can be computed very rapidly. Other control samplings have been tested; cases involving 3000 actuators sampled at 128x128 have been run easily on the SPARC workstations.
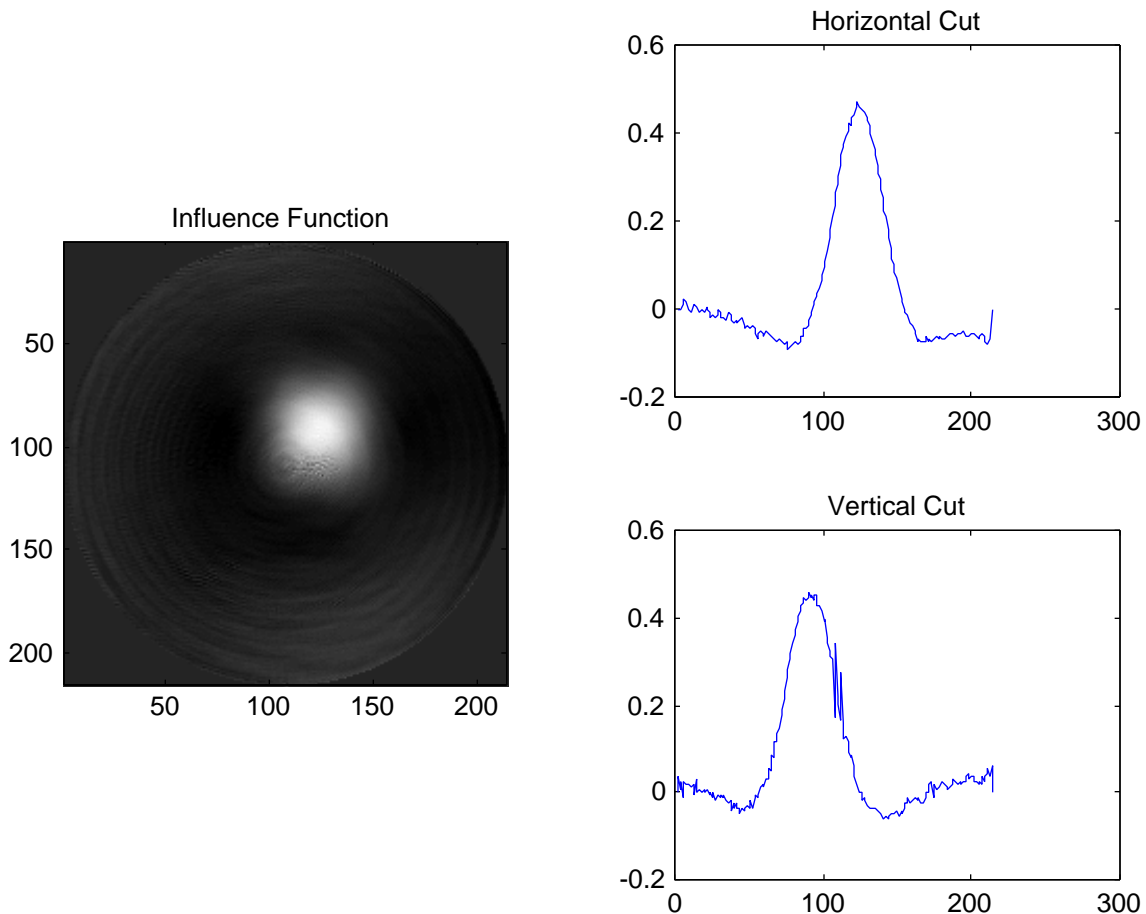

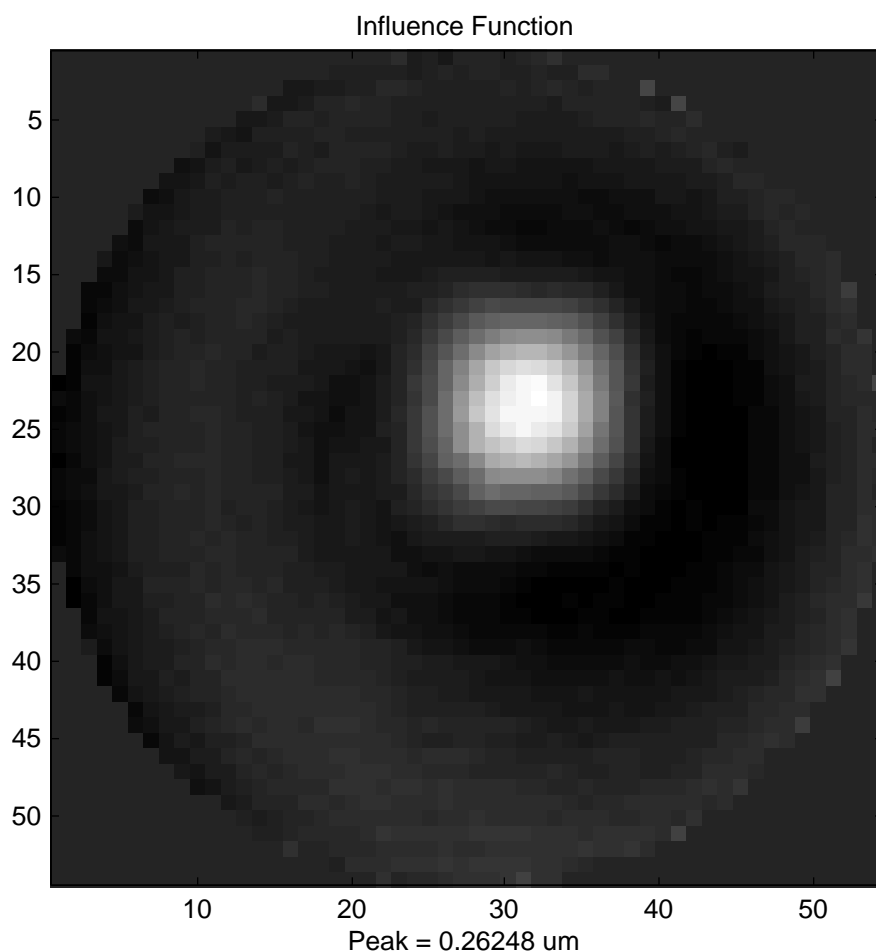**Figure 33. Influence function example**

Figure 34. Influence function at control sampling density

We found that once good influence functions hadbeen obtained, they remained quite stable, and did not require recalibration for the month or so that we had for this testing.

To provide an indication of the linearity and hysterisis characteristics of this mirror, we ran a sequence of poke tests, starting withno powerto the DM, andthen raising andlowering a single actuator through 2 or 3 loops. WF estimates were generated at severalpoints along the way. The influence function of the actuator was used as a basis for determining the displacementof the actuator from each estimate, giving a displacement vs. voltage plot shown in Fig. 35. As shown, the several curves nearly overly, but exhibit a strong quadratic nonlinearity. This test was run around the 0 voltage condition; the stroke curves flatten out abruptly for voltages greater than 30 or so.

The error in the displacement is also shown in Fig. 35, averaging less than 10 nm and peaking out at about 15 nm.

Further work is required, testing more of the DM actuators, and especially testing the AO DM actuators, to define the DM contribution to the overall DCATT error budget. This will be done after integration with the AO bench.
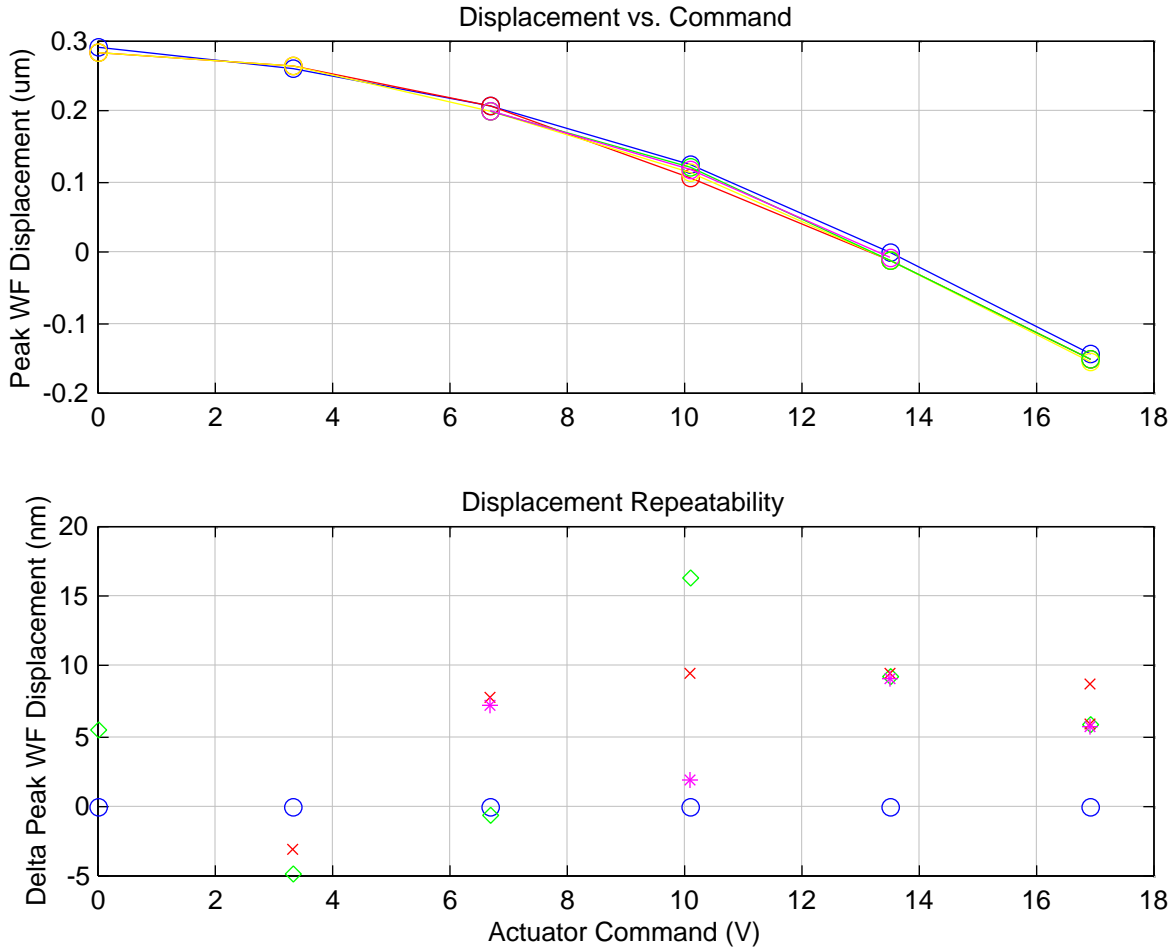
Figure 35. DM actuator displacement traces, showing nonlinearity and hysterisis
Figure 36. Return mirror and fl attened DM wavefronts

7. Detector performance

Detection noise is a factor in the overall WF sensing error, and so in the WF control error. It is relatively manageable for DCATT and NGST, as the WFC observations will use bright calibration sources, good detectors, multiple frames, dark frame subtraction, flat fielding, and long integration times. These options will help minimize the shot noise, read noise, dark current, flat fielding error, digitization, stray light, and other detection error sources.

Several simple tests were run mainly to confirmperformance of the CCD in the WFS camera and to help in suppressing stray light. These include quick looks at read noise, dark current, and stray light.

The first test was to determine read noise. Ten successive images were taken with 0 integration time, sothat there is no signal, and all of the received electrons represent noise. The results are shown in Fig. 37. There is a bias term of 109.2 DN, which has a frame-to-frame standard deviation of 3.7 DN. The average of all 10 frames is shown to be quite smooth, with a pixel-by-pixel standard deviation of 2.7 DN. The difference of 2 of these frames is shown in Fig. 38, again indicating typically small, Gaussian distributed noise with a standard deviation of 4.45 DN.

The next test was to estimate dark current effects. Images were taken with the camera shutter closed, over a range of integration times. Results are plotted in Fig. 39. As shown, mean dark current is low, but the

standard deviation is high.There appear to be a few very noisy pixels that run hot. The effects of these hot pixels is mitigated by the dark frame subtraction functions built into the Data Acquisition panel.
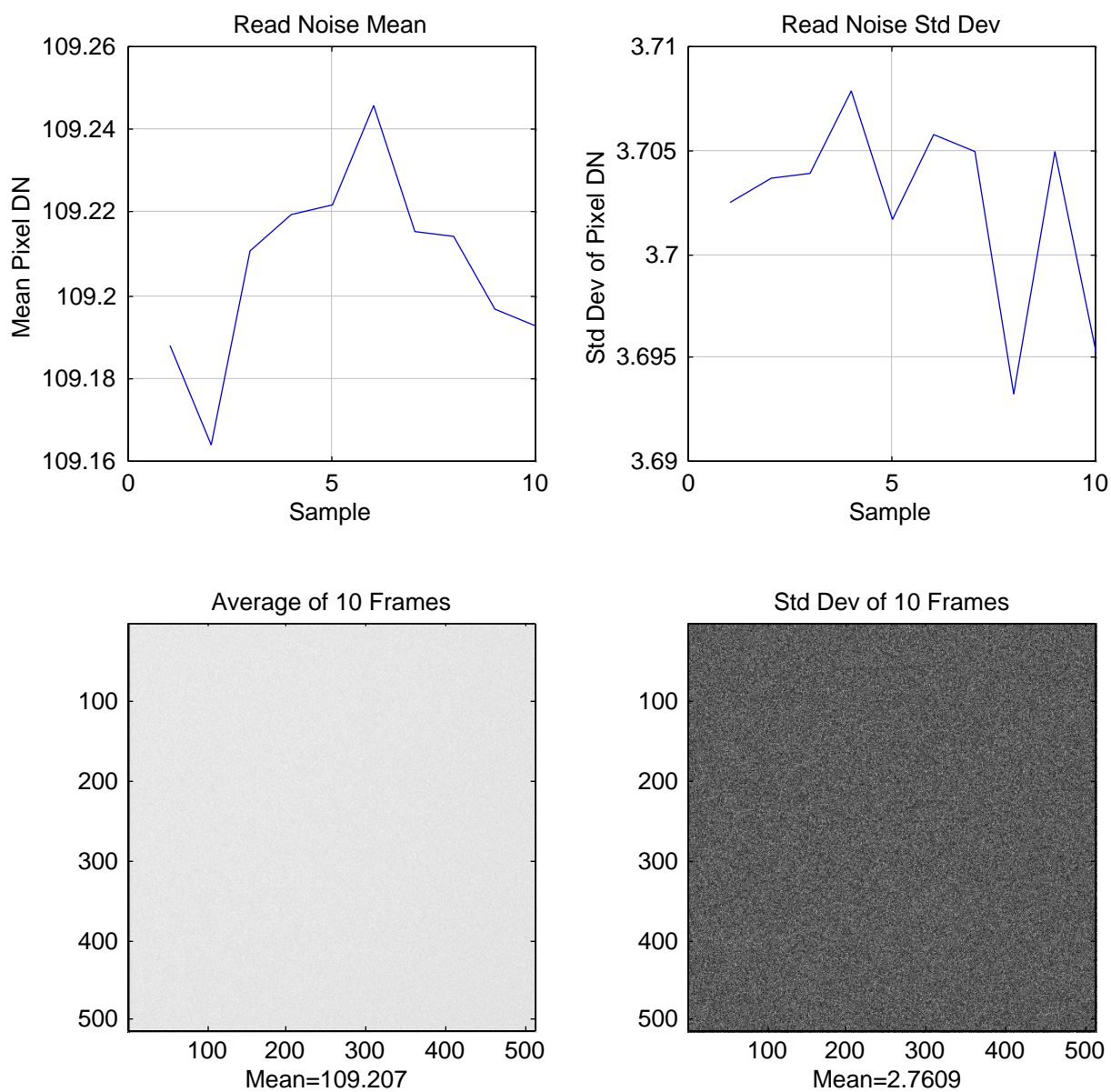

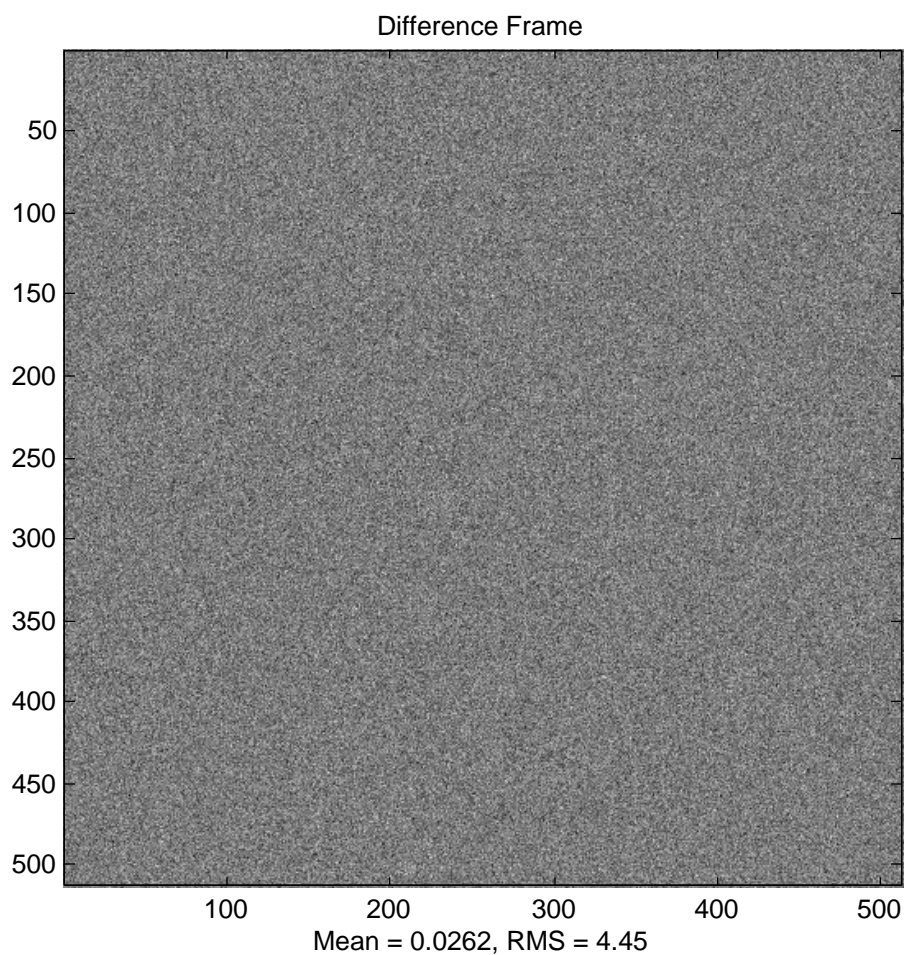**Figure 37. Read noise and bias from closed-shutter   , 0 time image frames**

Mean = 0.0262, RMS = 4.45

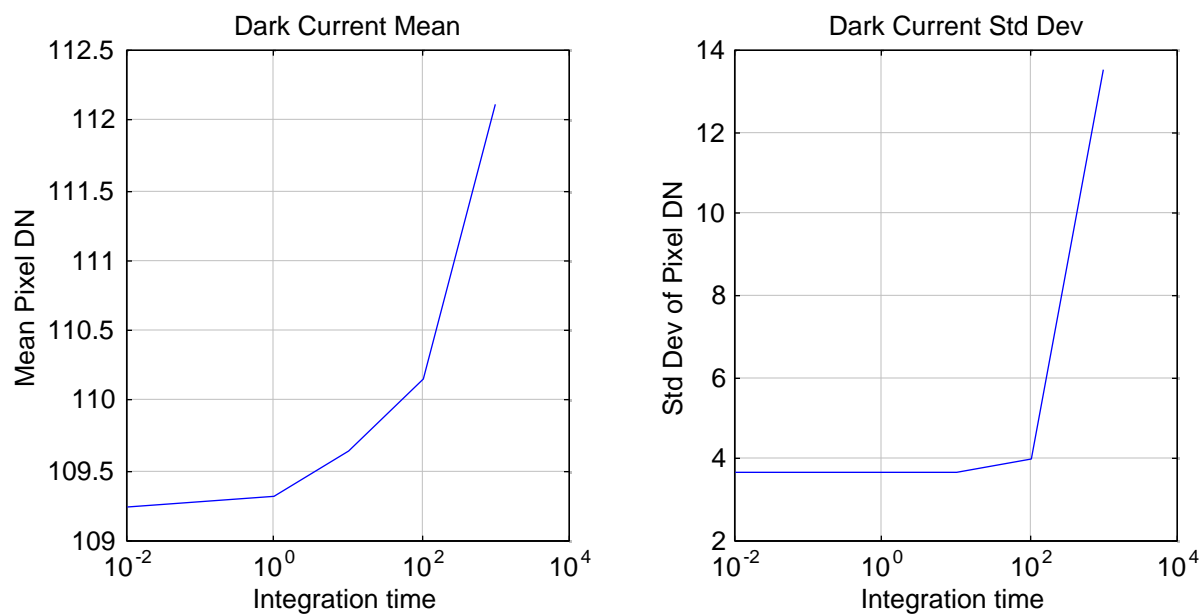**Figure 38. Difference of frame 1 and frame 2**

Figure 39. Dark current statistics vs. integration time, shutter closed.

The third set of tests address stray light. Two images were taken with the sources on but blocked between the 2 pinholes by a shutter. The Source and Simulator covers were on and the lab lights turned off. The camera shutter was open, allowing detection of light leaking into the detector by secondary light paths or from unmasked external sources.

The first frame (Fig. 40) was taken with the WFS pupil imaging lens out of the lightpath, which is the configuration used for focal imaging. Over the 2 minute integration time, the mean pixel value grew to a mean of 173 abovethe durk current value expected of about 111. The distribution is quite uniform across the512x512 image window. As in the dark current tests, several hot pixels were identified. These were zeroed in this dark frame, and can be identified as little black dots (the line is a plotting artifact).

Dark Frame, Shutter Open, No Pupil Lens, t=120 sec
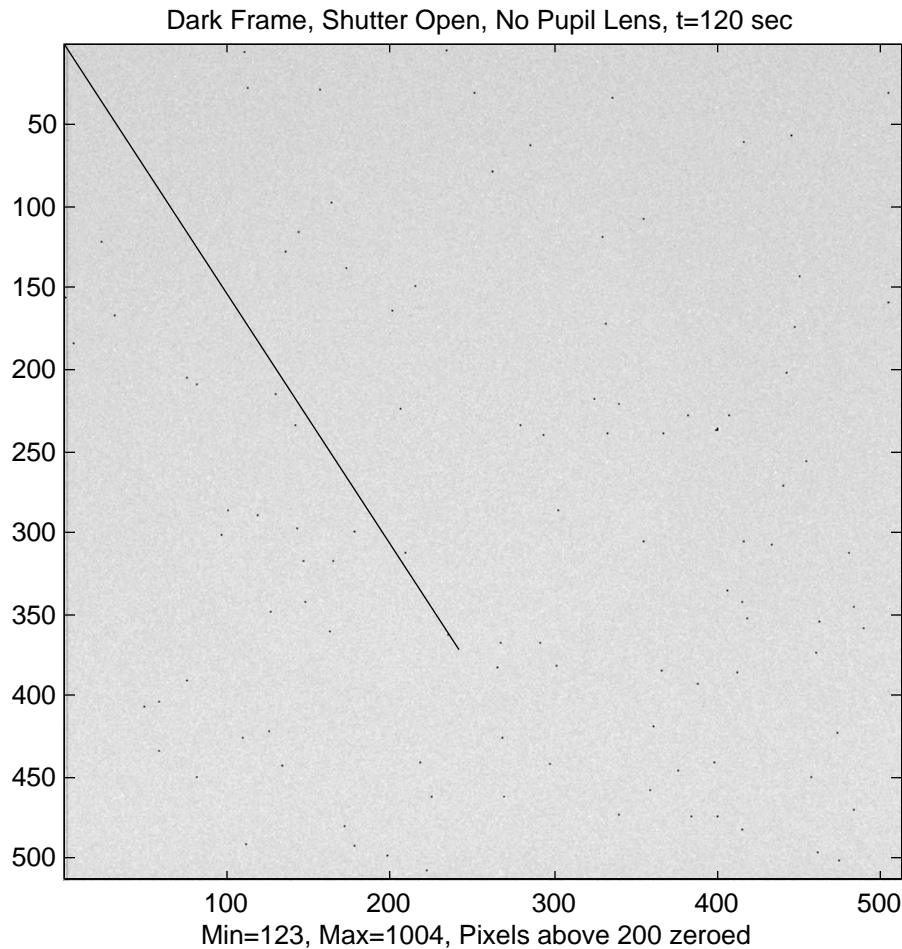
Min=123, Max=1004, Pixels above 200 zeroed

Figure 40. Dark frame, shutter open, no pupil lens. Shows stray light, dark current, read noise combined. Max = 1004, Min = 123, Mean = 173.7, Std dev = 6.41

The second frame was taken with the pupil imaging lens in place. The lens holder acts as an aperture, blocking some of the light incident on the detector. This is readily apparent in Fig. 41, which shows a region of concentratedillumination. Mean pixel value is lower, at 145 DN. Again, hot pixels were seen, with the hottest being zeroed in the plot.

These stray light images are fairly clean, which was not originally the case! First light dark frames had a significant number of artifacts, which prompted much experimentation with black cardboard and tape. This did not prevent good WFS operations, however. The current, fully enclosed modules are well controlled.

29

Dark Frame, Shutter Open, With Pupil Lens, t=120 sec
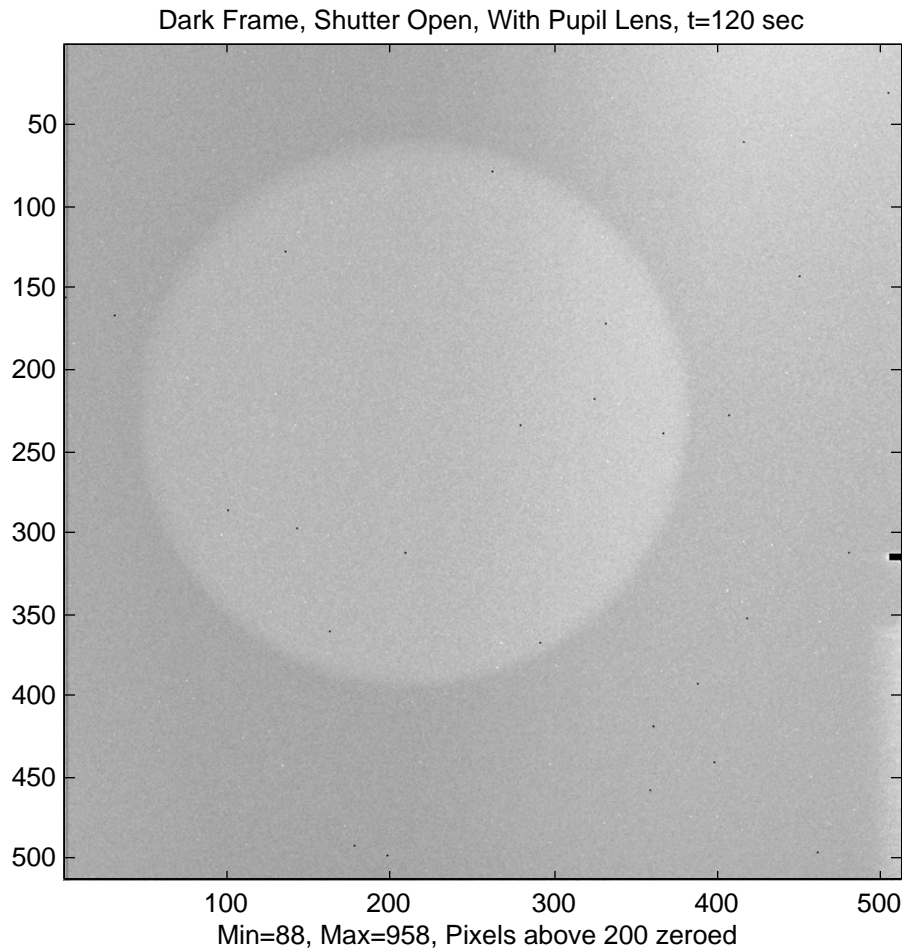
Min=88, Max=958, Pixels above 200 zeroed

Figure 41. Dark frame, shutter open, with pupil lens. Shows stray light, dark current, read noise combined. Max = 958, Min = 88, Mean = 145.5, Std dev = 10.5

8.   Conclusions

The testing done in this early phase of the DCATT project confirms that the Fine Phasing control planned for NGST has the accuracy and robustness needed to meet the needs of the project. WFS error was at the /100 level, and overall WFCat the /30 level, at 632.8 nm wavelength. This performance exceeds the basic DCATT requirement of /20 at 2 um wavelength.

9.   Data log

```
Overall log:
In chronological order:

first_light      Dec. 7-14          some sample data when the source was just set
                                    up
presentations    Dec. 14            panel snaphots for reports
influence_01     Dec. 30-31         First  stab  at  taking  influence  function
                                    data.Not a complete set.
influence_02     Dec. 31-Jan. 2     Influence functions, done 4 at a time
linearity_01     Jan. 4-6           Erroneous  set  of  data  attempting  to  measure
                                    nonlinearity and hystersis in actuators
```

```
flat_01           Jan. 6           Attempting to flatten mirror with influence
                                   functions in influence_02
influence_03      Jan. 7-9         Influence functions, done 1 at a time
flat_02           Jan. 11-13       Flattened astigmatism data
calibrate_01      Jan. 16          Data  using  different  number  of  averaged
                                   images to test dynamic range
linearity_02      Jan. 18          Erroneous linearity data
calibrate_02      Jan. 20-23       Good flattened data with Gain=98
linearity_03      Jan. 23-24       Pushed  up  actuator  #45  to  measure  DM
                                   linearity and hysteresis
noise_01          Jan. 28          Data for calculating dark and read noise
calibrate_03      Jan. 27-Feb. 3   Various  data,  comparing  phase  retrieval
                                   algorithm,  different  wavelengths,  laser,
                                   bypass mirror
newpinhole_01     Feb. 9           blackened 50 um pinhole
nopinhole         Feb. 10          no exit pinhole
newpinhole_02     Feb. 13          5 um pinhole back in
```

Directory calibrate_03:
The purpose of this directory is to take five data sets of the same thing
and see how closely phase retrieval matches the data.
The rms difference between the images are as follows:

```
                    02              03              04      05
01               0.0100          0.0107          0.01120.0109
02                               0.0120          0.01190.0116
03                                               0.01070.0104
04                                               0.0105
```

data_??k.mat is the data used for this initial test
est_01k.mat - est_05k.mat were centered using centroids
est_06k.mat - est_10k.mat were centered using thresholds
est_0?kk.mat are estimate done with all the image files using the same values
    for centering
data_??ll.mat have bandwidth=5.5 nm, interrupted
data_??l.mat
data_??mm.mat have bandwidth=20 nm, interrupted
data_??m.mat were taken with the red laser
data_??n.mat used 797 nm filter
data_??o.mat used simulator return (bypass) mirror
data_??p.mat used 513 nm filter
data_01q.mat highly aberrated, 633 nm
data_02q.mat highly aberrated, 514 nm
data_03q.mat highly aberrated, 795 nm
data_04q.mat highly aberrated, 650 nm
data_05q.mat highly aberrated, 670 nm

Directory calibrate_04:
```
dark_01.mat      120 sec. dark frame with no pupil lens (defocus = 25 mm)
dark_02.mat      120 sec. dark frame with pupil lens (defocus = 0mm)
data_01t.mat     First data, trying to flatten
data_02t.mat     flattened data_01t
data_??u.mat     flat wavefront
data_??v.mat     one actuator pushed
data_??w.mat     astigmatism (wrapped)
data_??x.mat     astigmatism
```

10. Acknowledgement

11. References

1. A. Lowman, "DCATT Source Design Document," in work.

2. A. Lowman, "OCC Software Manual," in work.

3. S.Basinger, "Executive Software User Reference," in work.

4. A. Lowman, "DCATT Simulator Design Document," in work.

5. A. Lowman, "DCATT Wavefront Sensor Design Document," in work.

6. DM description.

7. DM Electronics description.

8. D. Redding, et al, "NGST Baseline WF Control"

9. D. Redding, S. Basinger, "DCATT Algorithms Document," in work.